TRACKING AND CHARACTERIZATION OF MOVING ACOUSTIC SOURCES USING AN INFRASOUND ARRAY AT VOLCÁN SANTIAGUITO, GUATEMALA

by

Brian R. Terbush

A thesis

submitted in partial fulfillment

of the requirements for the degree of

Master of Science in Geophysics

Boise State University

August 2015

BOISE STATE UNIVERSITY GRADUATE COLLEGE

DEFENSE COMMITTEE AND FINAL READING APPROVALS

of the thesis submitted by

Brian R. Terbush

Thesis Title: Tracking and Characterization of Moving Acoustic Sources Using an Infrasound Array at Volcán Santiaguito, Guatemala

Date of Final Oral Examination: 05 December 2014

The following individuals read and discussed the thesis submitted by student Brian R. Terbush, and they evaluated his presentation and response to questions during the final oral examination. They found that the student passed the final oral examination.

Jeffrey B. Johnson, Ph.D.	Chair, Supervisory Committee
Hans-Peter Marshall, Ph.D.	Member, Supervisory Committee
Lee M. Liberty, Ph.D.	Member, Supervisory Committee
Brittany D. Brand, Ph.D.	Member, Supervisory Committee

The final reading approval of the thesis was granted by Jeffrey B. Johnson, Ph.D., Chair of the Supervisory Committee. The thesis was approved for the Graduate College by John R. Pelton, Ph.D., Dean of the Graduate College.

ABSTRACT

Active volcanic processes produce large amounts of acoustic energy within the infrasound band (0-20 Hz). Infrasound-sensitive microphones are often installed in addition to other forms of volcano monitoring equipment to increase the ability to remotely detect volcanic activity. In this study, an array of microphones was deployed without any additional sensor types for 36 hours at Santiaguito, Guatemala, to test the detection capabilities of a standalone microphone array. Array processing was applied to the recorded data, through frequency-domain beamforming and calculating a Fisher statistic (***F***). A changing ***F***-threshold value was applied to differentiate between desired detections, or signal, and acoustic energy not originating from desired sources, or noise. Through determination of signal backazimuth, and knowing the azimuthal ranges of expected events, detections were categorized into three potential sources: volcanic explosion, volcanic rock fall, or non-volcanic rock fall.

After characterizing a signal as one of the three event types, determination of relative occurrence of each event type showed that volcanic rock falls were the most common event through the deployment. Progression of signal backazimuth through time indicated movement of rock fall events. Explosion events were demonstrated to be non-moving as expected. Calculation of a spectral median frequency for these events, and comparison to signal backazimuth validates results of previous studies, that rock fall infrasound is characterized by higher frequencies than explosions. This method was

shown to be effective for remotely categorizing activity at a volcano during time periods of low wind.

TABLE OF CONTENTS

LIST OF TABLES

LIST OF FIGURES

LIST OF ABBREVIATIONS

PDC	Pyroclastic Density Current
ECM	Electret condenser microphone
PMCC	Progressive multi-channel cross correlation
VEI	Volcanic explosivity index
PDF	Probability density function
FFT	Fast Fourier transform
m	Meters
km	Kilometers
V	Volts
Hz	Hertz
s	Seconds

LIST OF SYMBOLS

v_a	Apparent velocity
c	Velocity of sound in air
S_H	Horizontal slowness
$S_{X,Y,Z}$	Slowness (horizontal x, horizontal y, vertical z)
p	Slowness vector, with components (S_X, S_Y, S_Z)
x_{ij}	Horizontal distance between stations i and j
t_{ij}	Time required to travel between stations i and j
F	Fisher statistic
ω	Angular frequency
θ	Azimuth
φ	Elevation angle
A	Amplitude of a Fourier transform
E_{SM}	Energy at spectral median frequency
f_{NYQ}	Nyquist frequency: one half of sample rate
f_{SM}	Spectral median frequency

CHAPTER ONE

1.1 Introduction to Volcano Infrasound

Volcanic environments produce a variety of infrasound sources. Infrasound is defined as acoustic energy, or pressure waves propagating through the atmosphere, with a frequency below 20 Hz. Sources of volcano infrasound include but are not limited to explosive eruptions (Johnson et al., 2003), gas jetting and "chugging," (Ruiz et al., 2006), pyroclastic density currents (PDC) (Yamasato, 1997), and rock falls (Moran et al., 2008). PDC refers to any gravity-driven flow event with a combination of hot gas, ash, and rock material.

Infrasound recordings at volcanoes also contain large amounts of energy not originating from volcanic sources. In this particular experiment, sound not arriving from expected source directions is considered noise. The noise component of infrasound records at volcanoes commonly contains wind. In mountainous regions, wind may originate from any direction, during any time of day. Noise in infrasound recordings may also originate from anthropogenic sources. Some common sources of anthropogenic noise are explosions, mining blasts, industrial equipment, vehicles, and aircraft (Evers & Schweitzer, 2011).

One method to mitigate the effects of noise sources is by deploying sensor arrays, instead of just one sensor (Almendros et al., 2002a; Rost & Thomas, 2002; Johnson et al., 2011, Johnson & Ronan, in review). With an array data may be compared between multiple records at once to determine more information about energy sources. Array

processing techniques can be used to determine the backazimuth, or direction to the source of incoming energy (Rost & Thomas, 2002). With arrays at volcanoes, backazimuth can be used to show from which part of the volcano a sound originated.

Arrays of instruments are commonly deployed to monitor volcanic activity. A minimum of three sensors is required to calculate a backazimuth. At Unzen Volcano in Japan, Yamasato (1997) detected the movement of a PDC using an array of seismometers. There was only one microphone in this deployment but through the acoustic record the study detected a Doppler Effect in infrasonic signal originating from the PDC. The Doppler Effect indicates that sound generation occurred at the propagation front (Yamasato, 1997). At Soufriere Hills Volcano, Montserrat, seismometers tracked PDCs in real-time and showed movement down the slope (Ripepe et al., 2010). PDCs at Soufriere Hills, were also recorded using a combination of infrasound and thermal images (Delle Donne et al., 2014). While acoustic sensors were part of each deployment, none of these studies used infrasound as the only monitoring equipment.

Remotely detecting rock falls at volcanic domes is beneficial to determining changes in their activity over time. A previous study at Soufriere Hills Volcano indicated that more seismic detections classified as rock fall events occurred during periods of high lava effusion (Luckett, 2002). Rock fall detections have also been used as a proxy for activity within the caldera of the Piton de La Fournaise shield volcano to monitor caldera wall stability (Hibert et al., 2014). If infrasound microphones alone are shown to be effective for rock fall detections, they may be used to remotely monitor volcanic activity and stability over long periods of time.

Use of infrasound microphones for monitoring has several benefits. Unlike cameras, microphones continue to record relevant information when the view of the volcano is obstructed, which is a common issue at volcanoes due to clouds. When compared to some other frequently-used monitoring equipment, such as seismometers and tiltmeters, the electret condenser microphones (ECMs) used in this experiment are inexpensive and easy to deploy. These microphones also have a low power consumption.

Volcanic domes are associated with a rock fall activity. This is particularly true of domes where a lava flow is present. Rock falls often begin at the front or along the edges of the lava flow, and tumble down the sides of the dome. Monitoring volcanic dome activity is critical to hazard mitigation. Soufriere Hills Volcano, mentioned earlier for its dome and common rock falls, is an example of a dome with a high hazard (Carn et al., 2004). Other volcanic domes with a high hazard potential due to being close to population centers, and having historic dome-collapse events, include Merapi, Indonesia (Hort et al., 2006), and Unzen, Japan (Okuno et al., 2001). Montitoring activity at volcanoes like these examples helps to mitigate their hazards.

The ability to remotely monitor the locations and paths of rock falls could also potentially be used to make closures and cleanup more efficient for mountain roadways. Infrasound monitoring has been shown to be effective for remote snow-avalanche detection in mountain highway corridors (Havens et al., 2014). Due to a guaranteed source of rock falls during this deployment, this study examines whether rock falls may be detected, tracked and characterized using only an infrasound array.

1.2 Santiaguito Background

Guatemalan and Central American volcanism is the result of active tectonic plate subduction. Along the southwest coast, the Cocos plate of the Pacific Ocean is subducting beneath the Caribbean plate at a rate of 7-8 cm/year (Singer et al., 2011). The trench associated with this subduction has produced several large earthquakes. Most of Guatemala's active volcanism occurs inland from this plate boundary, as part of a region known as the Central American Volcanic Arc. Several composite volcanoes in this arc have produced large explosive eruptions, such as Volcan de Fuego and Santa Maria Volcano in Guatemala. Santa Maria's 1902 eruption had a Volcanic Explosivity Index (VEI) of 6, with a cumulative volume of 5 km^3 erupted material, placing it as the third-largest volcanic eruption in the 20th century (Rose, 1987). This eruption began under the southwest flank and removed most of the volcanic edifice, leaving behind the crater where the Santiaguito dome complex is today (Figure 1).

Santiaguito is a complex of four dacitic volcanic domes which extruded following Santa Maria's eruption (Rose, 1987). Due to its accessibility (Figure 1) and generally reliable behavior, the domes have been studied using a variety of geological and geophysical methods. The domes are made of dacite lava, compositionally similar but volatile-poor compared to the lava erupted in 1902 (Singer et al., 2011). Eruptive products show a gradual decrease in silica content through time (Scott et al., 2013). Satellite imagery and field data determined that lava effusion periods at Santiaguito are cyclic in nature, showing periods of relative high and low lava effusion (Harris et al., 2003).

Figure 1. Santiaguito and Santa Maria, Guatemala. Santiaguito is the small dome in the foreground at the base of Santa Maria (elevation 3740m a.s.l.). The city of Quetzaltenango (pop. 200,000) is in the valley to the north. Location of the array in the crater is marked by the "+." (Source: "Santiaguito." 14°45'12.45" N and 91°33'08.73" W. Google Earth. 1/18/2014. 11/4/2014.)

After 20 years of inactivity following Santa Maria's paroxysm, the Caliente dome began extruding in 1922. Caliente's growth continued until its collapse in 1929, which resulted in a large block and ash pyroclastic flow (Rose, 1987). After 1929, eruptive activity resumed, building three more domes known as La Mitad, El Monje, and El Brujo, which are currently inactive. Since 1977, eruptive activity has been focused at Caliente (Bluth & Rose, 2004). Caliente's current activity is characterized by a repeating temporal trend. Effusive dome-forming eruptions occur contemporaneously with small explosive eruptions for 3-5 years of higher lava flux. This is followed by 5-7 years of relative quiescence (Harris et. al, 2003).

Santiaguito activity during the November 2012 deployment incuded a blocky lava flow erupting from Caliente's summit, and small explosions of gas and ash, which occasionally resulted in PDCs. The lava flow is located on the southeast side of the dome, and is a source of rock falls, as rocks break off the advancing front and tumble down the sides (Harris et al., 2002). Rock falls unrelated to active volcanism are also common on the 1400-meter crater scarp of Santa Maria's old volcanic edifice (Holland, 2011). Due to the common occurrence of rock falls from both source areas, the area within the crater of Santa Maria Volcano provides an excellent field laboratory to study these moving events.

1.3 Previous Rock Fall Studies

Previous research on rock falls tends to focus on their seismic signal, but several studies have also included acoustic records. Since rock falls are common at active lava domes, most rock fall studies occurred at volcanoes with these features. Studies of long-term activity at Soufriere Hills Volcano in Montserrat included a pressure sensor, which detects infrasound in the same manner as a microphone. The pressure sensor's traces were used to establish that there is often a burst of outgassing from the dome prior to the main rock fall signal (Luckett, 2002). Luckett characterized rock fall signals as emergent, beginning with a low amplitude, and progressing to a higher amplitude for the main portion of the signal. This study also showed that seismic waveforms from rock fall contain the greatest energy in the frequency band between 2 and 8 Hz, but some contain a 1-2 Hz signal at the beginning associated with outgassing.

Observers recorded a large rock fall on the lava dome at Mount Saint Helens using both seismic and infrasound signal (Moran et al., 2008). This rock fall generated a

large plume of dust, initially causing it to be mistaken for ash from an explosive eruption. The infrasonic and seismic records, however, contained only emergent acoustic signals, which are not associated with explosion waveforms. Instruments recorded a long drawn-out period of high infrasonic and seismic amplitude with a cigar-shaped waveform before the ash began to rise. The waveform from this rock fall is a higher-amplitude version of expected rock fall signal from the Caliente dome.

Rock fall studies were made at Santiaguito using a 3-element microphone array and seismic sensor in January 2014 (Johnson & Ronan, in review). This study identified rock fall events, tracked their location and calculated their velocities. It confirmed several rock fall events and their movement paths with simultaneous video camera observation. The study also determined that the frequency content of rock fall events is higher than that of volcanic explosions, using a spectral centroid to compare the two.

Volcanic rock falls do not only occur at domes. Another study performed at the Piton de la Fournaise shield volcano, Reunion Island, detected rock falls using seismic data (Hibert et al., 2014). Hibert et al. compared several methods to develop the most robust automatic picking algorithm for rock fall events. Based on this study, changes in kurtosis, a statistical representation of waveform amplitude asymmetry, are the most accurate way to separate rock falls from background in a seismic waveform record. Rock falls at Piton de la Fournaise indicate instabilities along the crater walls.

CHAPTER TWO: EXPERIMENT AND METHODS

2.1 Deployment

In November 2012, I deployed an array of eight ECMs along a flat section of ground 840 m east, 200 m in elevation below Caliente's vent, and 2000 m SW, 1400 m in elevation below Santa Maria's summit (Figure 2). Microphones were placed around the central microphone and data logger, at distances alternating between 15 and 33 meters, based on microphone cable lengths (Figure 3). ECMs recorded to a Dataq DI-710 8-channel, 14-bit digitizer at a sample rate of 100 Hz. ECMs are notable for having a low noise-floor, meaning that instrument noise has minimal effect on recorded waveforms. The low noise-floor is beneficial for the detection of low-amplitude signals such as rock falls.

An issue with ECMs is a low frequency roll-off. The mass-produced type of ECMs used in this deployment have a variable corner frequency from 1 to 5 Hz (Johnson et al., 2003). Below the corner frequency, recorded amplitudes begin to decrease. This means that if all 8 microphones record a 3 Hz signal from the same source, it may be recorded with different amplitude on each channel. As a result of this variability between microphones, and many signals of interest having frequencies below 5 Hz, calibration to a definite pressure value is not available within this dataset. While waveforms in other infrasound studies of volcanoes are typically reported in pascals, I represent waveform amplitude using a relative scale.

In order to maximize detections of low-amplitude signals, such as rock falls, the gain on the digitizer was set to 1000. Clipping of some stronger signals occurred, due to the voltage produced by the microphones being too high for the digitizer to record. Data values are normalized to the clipping amplitude of 0.01 V. While seven of the microphones generally displayed consistent amplitudes, the record from the microphone on channel 7 was often higher than the other channels, and higher than 0.01V. The data lost above this value would cause inaccuracies when data is processed. To avoid this, I removed data from channel 7 from the waveform record before processing. For the remainder of the experiment, I refer to the array as a 7-element array.

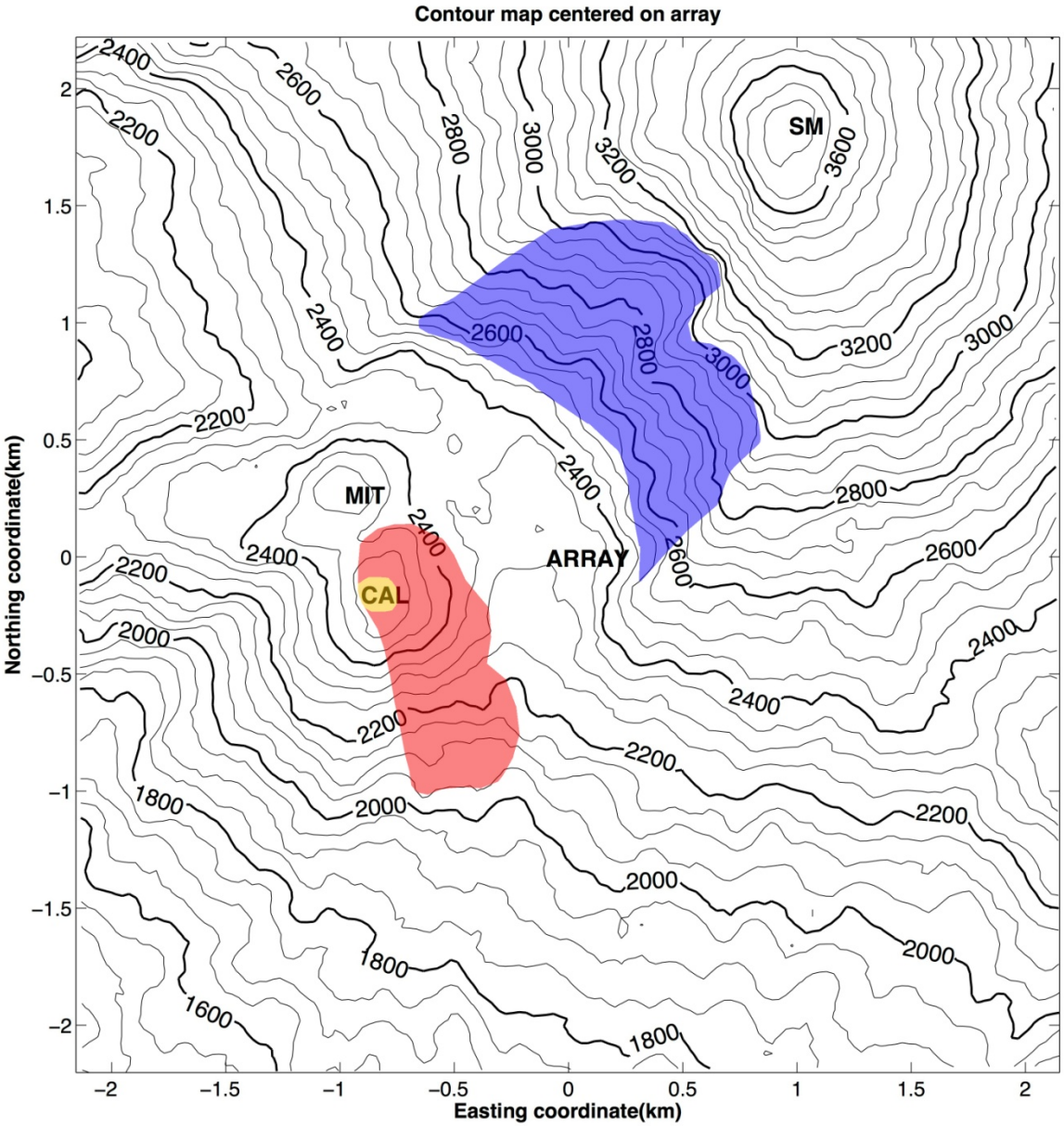

Figure 2. Map of deployment area, centered on array. Labeled points include the array, Caliente (CAL), inactive dome Mitad (MIT), and Santa Maria (SM). The steep slopes to the west of Santa Maria (Blue) and south and east of CAL (red) are candidate sources for rock falls. Caliente's crater (yellow), the potential source for explosions was roughly 120 m in diameter at the time of deployment.

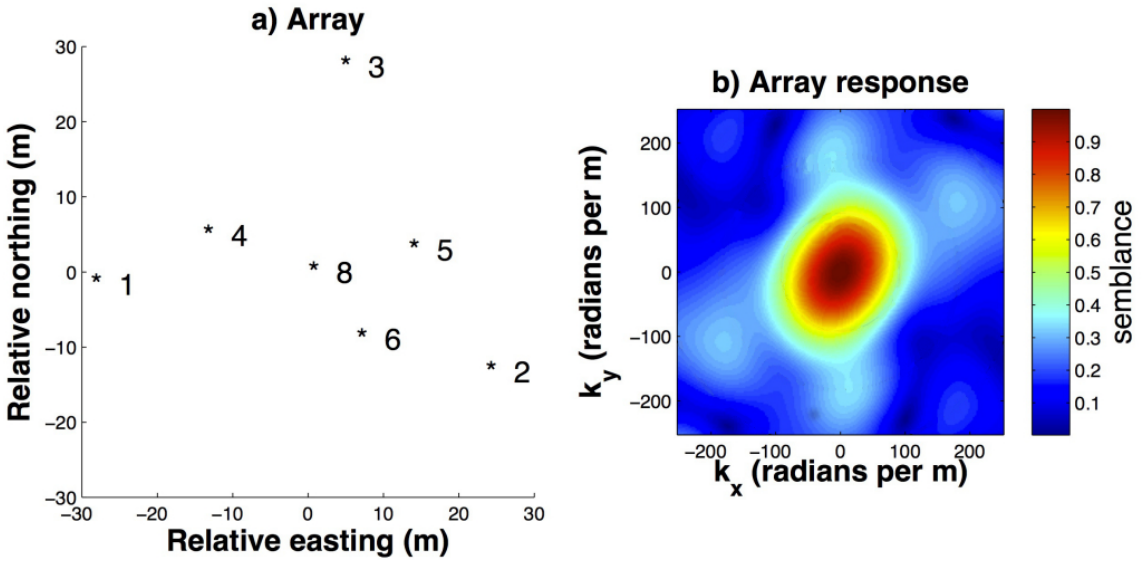

Figure 3. Array configuration and response. a) Positions of microphones with channel number labeled. b) Array response of the Santiaguito configuration. Semblance, shown on the colorbar, describes the strength of signal. Azimuths from 0 to 360 degrees are clockwise around the circle, starting from north. A central circular shape, and lack of high-semblance sidelobes indicates a robust array configuration for resolution of incoming signal.

Figure 3 shows the configuration and array response of this deployment. Array response is an established theoretical method to show how a given array configuration will be able to make detections based on incoming source direction (Rost & Thomas, 2002). The shape of the array response diagram reflects from which directions incoming energy will be most coherent across the array. If an incoming energy distribution existed, it would appear as sidelobes on the diagram (Rost & Thomas, 2002). The circular shape indicates that the direction of incoming energy will not have an effect on the amplitude of recorded waveforms.

Recording began at 2:32:00 UTC on November 12th, 2012, and continued for 36 hours. During the deployment, small explosive eruptions occurred approximately every 0.5 to 2 hours. Several of these eruptions resulted in small PDCs. Many rock falls also originated from the lava flow near Caliente's vent. Deployment began 5 days after a

magnitude 7.4 Earthquake, November 7th, 2012, at 16:35:46, UTC (NEIC, 2012). The epicenter was 24 km deep, 90 km SSW of Santa Maria. During the deployment, the field crew experienced aftershocks, later determined to be magnitudes 5 to 6. Rock falls from Santa Maria are a noted common occurrence (Holland et al., 2011), but it is likely that this seismic activity resulted in an increased number of rock fall events during the deployment period.

2.2. Methods

2.2.1 Waveform Observation

I began analysis with visual observation of the waveform record. Helicorder-style plots are effective for summarizing large time intervals of acoustic or seismic data on a single plot (Figure 4). During the first 12 hours of deployment (Figure 4a), the data contain several clear, short duration, high-amplitude waveforms. Based upon similarities with previous recordings at volcanoes, these waveforms are hypothesized to be volcanic explosions (Johnson et al., 2011). Explosions during the 2012 deployment occurred approximately every 0.5 to 2 hours, consistent with recent studies (e.g., Holland et al., 2011; Scott et al., 2013; Johnson & Ronan, in review). These records also show low-amplitude emergent waveforms. These could represent rock fall, as they are similar in shape to other observed rock fall waveforms (Luckett, 2002, Moran et al., 2008). Further analysis using array processing methods will confirm these event classifications.

Another waveform shape appearing in this record is characterized by extended periods of high-amplitude (Figure 4b). These waveforms are distinct from the hypothesized explosion and rock fall signals in that they are high-amplitude and frequently clipping, as shown by their flat top. These waveforms also lack any

discernible characteristic shape, when compared to waveform examples seen in Figure 4a. Array processing reveals that these waveforms do not come from a volcanic direction, and are thus considered noise. Hours 28-32 on Figure 4b correspond to a time of high winds during the second night. Wind is a common source of acoustic noise in volcanic environments (Garces et al., 1998).

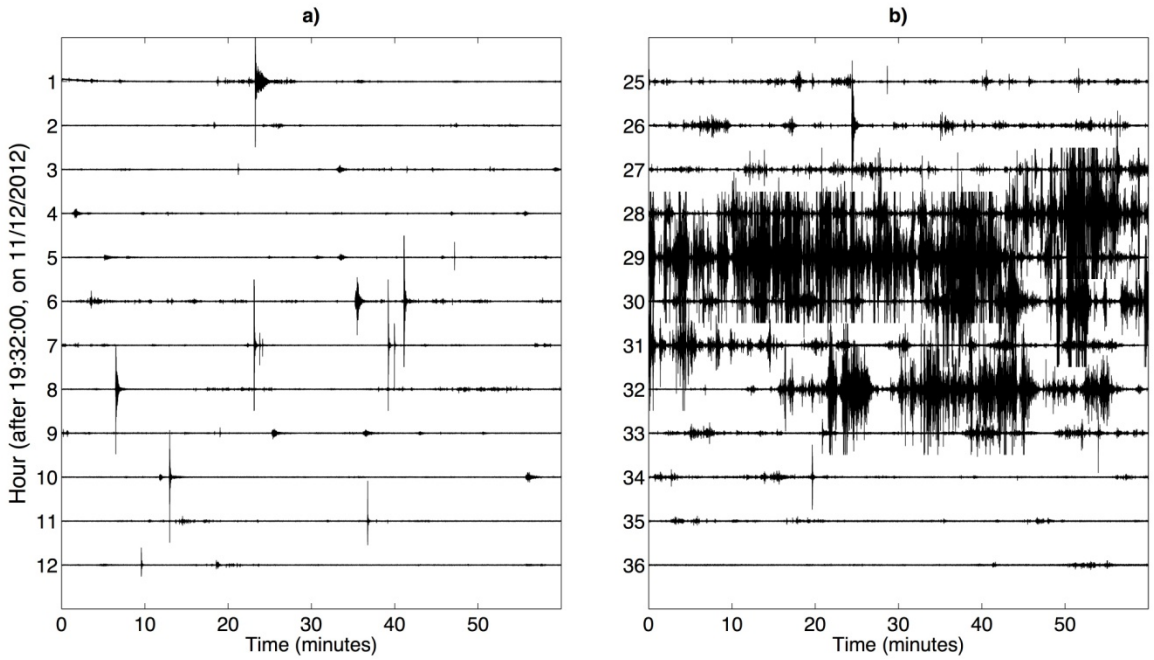

Figure 4. Helicorder-style plots for 12-hour periods of data. Relative amplitudes are shown for a) the first 12 hours of deployment, with low winds, and b) the last 12 hours of deployment, characterized by high winds.

The 7-element array at Santiaguito identifies passage of coherent acoustic energy. Plane wave acoustic energy travels across the array and an apparent velocity is calculated. Apparent velocity v_a is the observed horizontal moveout velocity of sound, calculated based on the horizontal distance, x_{ij} between microphones i and j, and the time, t_{ij} it takes to travel between them, where $v_a = x_{ij}/t_{ij}$. This is not the same as the intrinsic velocity of sound in air, c, because apparent velocity changes based on the orientation of incoming acoustic energy. The horizontal slowness, S_H, for an incoming pressure wave

is the inverse of $\boldsymbol{v_a}$. A signal moving horizontally across the array, without any inclination, has $\boldsymbol{S_H}$ equal to the intrinsic slowness of sound in air, or $1/\boldsymbol{c}$. Waves arriving from angles above the horizontal will take less time to travel between two microphones and have a higher $\boldsymbol{v_a}$ than the speed of sound. A plane wave arriving from directly overhead has an infinite apparent velocity, since it is recorded at all stations simultaneously.

For a given plane wave, coherent acoustic energy is observed at moveout times, which are predictable for a given array geometry (e.g., Figure 5a). Predicted moveout times equal $\boldsymbol{S_H x_{ij}}$. Wind crossing the array generally has a lower velocity than sound waves and is not coherent across distance scales of meters (Figure 5b).

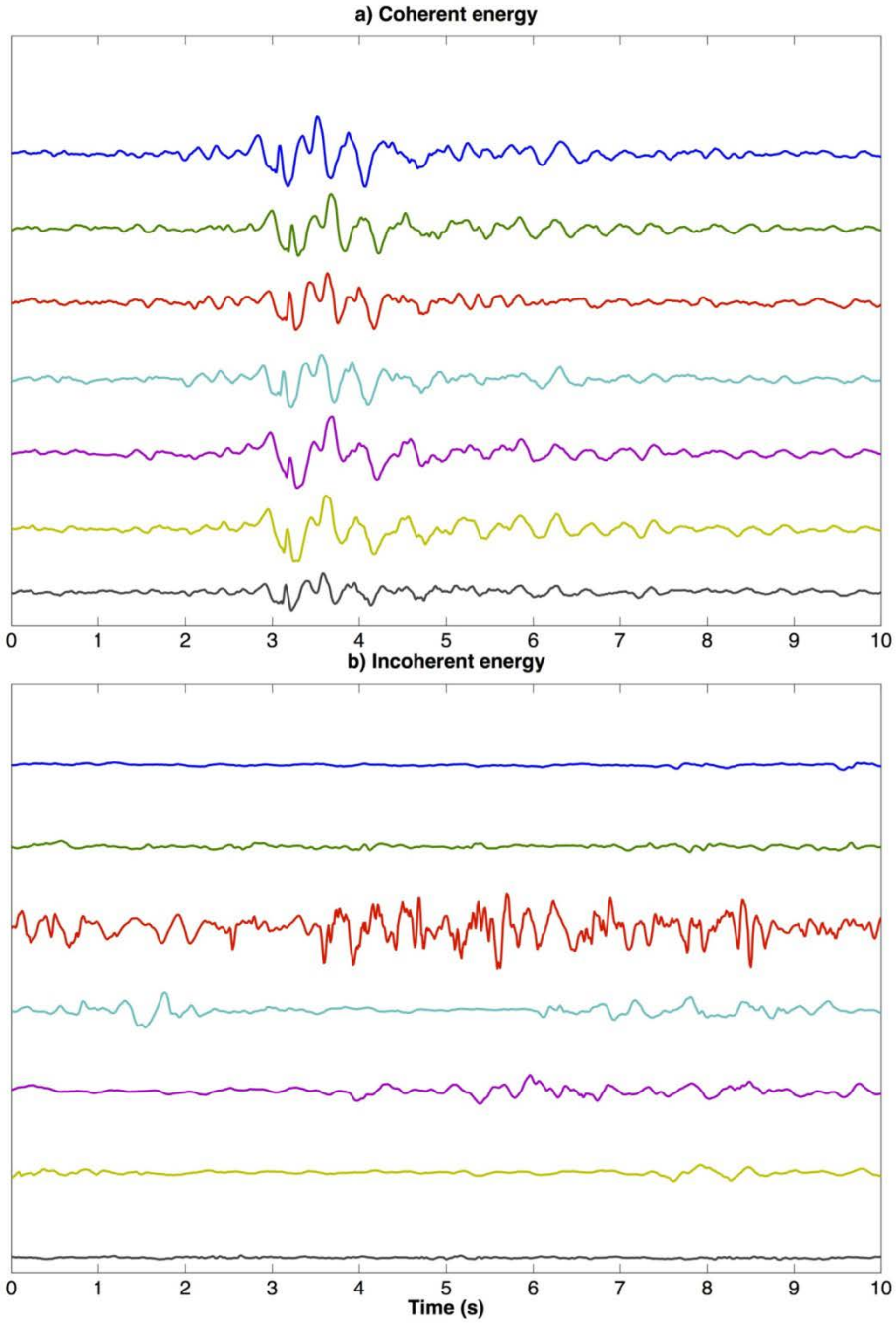

Figure 5. Ten-second windows showing waveforms across all channels. a) Panel showing coherent energy, where the order in which the main wave arrives at stations may be observed. b) Incoherent waveform record, where there is a lack of similarity between all waveforms across the array, and no value of time lag will successfully cause the waveforms to line up.

I characterized coherent infrasound signal from Caliente as either an explosion or a rock fall based on relative amplitude and duration. Coherent signal from the direction

of Santa Maria is classified as rock fall. There are also coherent waveforms arriving from directions not associated with active areas. These are characterized as noise, despite being coherent. The initial distinction used to separate signal and noise in this experiment is whether the waveforms are from a volcanic or rock fall origin. Energy not originating from the direction of Santa Maria or Caliente does not meet these criteria.

Signals clearly identified as explosions have high normalized amplitudes (0.5-1.0) and durations of less than 10 seconds. Rock fall signals have medium-to-low normalized amplitudes below 0.5 and typical durations within a range of 20-180 seconds. Despite their characterization as 'rock falls,' the shape of these events is commonly observed in both seismic and infrasonic waveforms from volcanoes. Potential origins include PDCs (Delle Donne et al., 2014), gas venting (Ruiz et al., 2006), or rock fall from either Caliente or Santa Maria (Moran et al., 2008). Further processing is necessary to determine which specific type of event produced these signals.

To distinguish between a fixed-position (e.g., explosion or degassing) and a moving (e.g., rockfall or PDC) source, I used beamforming through incremental time windows. Beamforming is a calculation to determine the statistical likelihood that energy is arriving from any point on a grid of potential sources during a given time window. Beamforming is an appropriate technique as long as the array is planar (Rost & Thomas, 2002). It is reasonable to assume that this array is planar, as elevations vary by less than 4 meters across an aperture of 60 meters. Array aperture is also small compared to distance from the source. The array deployment site is gently sloped, but flat overall.

Beamforming is frequently used to determine source directions in both seismic and infrasound array processing (Rost & Thomas, 2002). For example, Almendros et al.

(2002a) used beamforming to locate a seismic source with changing backazimuth at Kilauea volcano. While the continuous seismic signal was initially thought to be volcanic in origin, evidence from beamforming compared on two arrays suggested that the signal most likely originated from a vehicle moving along the Crater Rim Drive. Ripepe's study (2010) tracked the fronts of moving pyroclastic flows at Soufrierre Hills Volcano. Havens et al. (2014) tracked the propagation of a snow avalanche using an array of infrasound microphones. Caljé (2005) used an acoustic array at Mt. Etna, and used beamforming with two different methods: Fisher's Statistic (***F***) calculation and the progressive multichannel cross correlation (PMCC) method (Cansi, 1995).

The PMCC method divides a seismic or infrasound array into 3-element sub-arrays. Beamforming is performed using one sub-array. Once coherence values for this initial array are calculated, a second array is chosen, and coherence analysis is performed again for the area of highest coherence. This method decreases the search area each time, effectively increasing resolution. The search process continues until the calculated coherence measure stops increasing. While PMCC is commonly used in array analysis, Caljé's work determined that ***F***, as defined by Melton and Bailey (1957), was a more robust method for detecting events in areas with higher ambient noise. As a result, I chose to use the ***F*** statistic method at Santiaguito. Most rock falls are low amplitude signals, so the ***F*** statistic method will increase the number of rock falls detected.

2.2.2 Coherence Analysis

To form beams, a grid of possible slowness values is created to test a number of possible wave incidences. Each point on a 42 x 42 grid has an associated horizontal slowness, corresponding to a specific slowness vector, $\boldsymbol{p}$. The slowness vector has components $\boldsymbol{S_X}$ and $\boldsymbol{S_Y}$ of horizontal slowness in the east-west and north-south directions, respectively, and vertical slowness $\boldsymbol{S_Z}$. Each $\boldsymbol{p}$ also has a defined backazimuth, θ measured in degrees clockwise from north. $\boldsymbol{S_X}$ and $\boldsymbol{S_Y}$ are defined using the horizontal slowness and azimuth by:

$$\boldsymbol{S_X} = \boldsymbol{S_H}\left(\sin(\theta)\right) \tag{1}$$

and:

$$\boldsymbol{S_Y} = \boldsymbol{S_H}\left(\cos(\theta)\right) \tag{2}$$

where $\boldsymbol{S_H}$ is the inverse of $\boldsymbol{v_a}$. Calculation of backazimuth for each point on the grid is performed using $\boldsymbol{S_X}$ and $\boldsymbol{S_Y}$ in the equation:

$$\theta = \tan^{-1}\left(\frac{\boldsymbol{S_X}}{\boldsymbol{S_Y}}\right) \tag{3}$$

These horizontal slownesses may then be used to recover $\boldsymbol{S_Z}$ and corresponding elevation angles of incident acoustic plane wave energy. This calculation requires $\boldsymbol{c}$, the adiabatic sound speed in air. This is calculated using:

$$\mathbf{c} = \sqrt{\gamma_g \boldsymbol{R} \boldsymbol{T}} \tag{4}$$

where $\boldsymbol{\gamma_g}$ is the adiabatic gas constant, $\boldsymbol{R}$ is the gas constant for air, and $\boldsymbol{T}$ is the temperature in Kelvins (Garces et al., 1998). The value of $\boldsymbol{\gamma_g R}$ is constant for air at 402.8

$m^2s^{-2}K^{-1}$ so the only variable that changes in this equation is air temperature. Temperatures in the field during our deployment ranged from roughly 5-20° C. Corresponding to these temperatures, a low slowness of 2.92 s/km and a high slowness of 3.03 s/km were calculated. For calculations within the experiment, I used a mean value between the two of 2.97 s/km.

I calculated the range of possible values in elevation angle due to differences in $\boldsymbol{c}$ in order to understand potential error in this measurement. Figure 6a compares high and low values of slowness (based on $\boldsymbol{c}$ at maximum and minimum temperatures), and indicates that there is a larger potential discrepancy between the two speeds at lower angles. This is because horizontal distances traveled across the array are greater when the elevation angle is closer to zero. Differences in velocity have a greater influence over longer distances. At higher elevation angles, horizontal slownesses approach zero and differences between the two slownesses become negligible.

Elevation angle, φ, is the angle between the plane of the array and the source of sound. Elevation angle is related to apparent slowness by

$$\phi = \cos^{-1}(\boldsymbol{S_H}\,\boldsymbol{c}) \tag{5}$$

For a given time window, I calculate $\boldsymbol{F}$ for each vector on the slowness grid. $\boldsymbol{F}$ is a quantitative value representing the statistical likelihood that signal originates from a given slowness vector on the grid. In the time domain, $\boldsymbol{F}$ is defined as the variance of signal divided by the variance of noise within a discrete time window (Melton & Bailey, 1957; Caljé, 2005). Variance is a statistical representation of the spread between data values. Higher variance occurs where there is a greater difference between values. Signals that are in-phase sum constructively, increasing total amplitude in both the

positive and negative directions. Stacked signals with higher summed amplitude have a higher variance, because there is a greater spread between maximum and minimum values. When waveforms from noisy periods are shifted and summed, they interfere destructively, resulting in a low variance. Dividing shifted and stacked signal variance by variance of the unshifted, stacked waveforms in the same window results in a high value of ***F***.

For an example of how ***F*** calculation works, refer to the waveforms from Figure 5. To calculate ***F***, each channel has an associated shift for each point on the slowness grid associated with the slowness of sound. Since the signals come from a coherent source direction based on ***c***, one or more values on the grid will allow the signals sum in-phase. This results in a higher value of ***F*** at these slownesses on the grid, which will give the most likely backazimuth and elevation angle of that waveform. When beamforming is performed on the waveforms in Figure 5b, the signals will not line up well with any time shift, resulting in low ***F*** at all points on the slowness grid.

In the frequency domain, an appropriate analogue for ***F***, as defined by Smart and Flinn (1971), is:

$$\mathrm{F} = \frac{E(\omega, p)}{\mathrm{E}(\omega) - \mathrm{E}(\omega,\mathrm{p})}(I - 1) \tag{6}$$

where $E(\omega,p)$ is the spectral energy at a point with frequency ω , with I microphones in the array. $E(\omega)$ is the total energy at angular frequency ω (Smart & Flinn, 1971). Each ω within the given band has an associated phase shift. Energy values in Equation (6) and their associated phase shift are defined by:

$$\mathbf{E}(\omega, \boldsymbol{p}) = \left(\frac{1}{I}\sum A_j(\omega)\, e^{-i\omega \boldsymbol{p} r_j}\right)^2 \quad (7)$$

and

$$\mathbf{E}(\omega) = \frac{1}{I}\sum \left(A_j(\omega)\right)^2 \quad (8)$$

where $\boldsymbol{r_j}$ is the position vector of microphone $\boldsymbol{j}$ from the array origin in meters, and $\boldsymbol{A_j(\omega)}$is the amplitude of the Fast Fourier Transform (FFT) at $\boldsymbol{\omega}$. This calculation phase-shifts the energy for a given frequency with the associated position in slowness space. Energy is summed across all channels, stacking the signal. In the cases of both $\boldsymbol{E(\omega,p)}$ and $\boldsymbol{E(\omega)}$, energy is averaged over the number of channels. The differences in energy between these two calculations serve as an analog for variance in signal and noise.

In this way, each $\boldsymbol{p}$ that makes up the slowness grid has an associated set of vertical and horizontal slownesses, backazimuth, and after this calculation, $\boldsymbol{F}$. Computation is performed in the frequency domain for the purpose of comparing signal coherence as a function of frequency. I hypothesize that rock fall signal and volcanic signal contain different frequency components. Performing the slowness search within different frequency bands can confirm this hypothesis.

2.2.3. Signal Differentiation

I performed the beamforming search across the entire 36-hour record, in order to calculate $\boldsymbol{F}$, backazimuth, and apparent velocity of each window. I used window lengths of 5, 10, and 30 seconds, with 50% overlap, to ensure that signal between two windows is analyzed. To test different frequency bands for incoming energy differences, I calculate $\boldsymbol{F}$ in both the full infrasound band from 0.25-20 Hz, and also from 2-8 Hz, for each

window length. The 2-8 Hz frequency band contains the most rock fall energy according to Luckett's (2002) study at Montserrat.

Figure 6 (panels b, c, and d) shows example beamforming solutions calculated for three different event types. I show these three particular events multiple times, as examples of how certain signals appear in slowness space. All three of these events are shown with $\boldsymbol{F}$ calculated in the 0.25-20 Hz frequency band. Energy originating from the old volcanic edifice of Santa Maria, or from an azimuth of -45-95°, is non-volcanic rock fall (Figure 6d). Signal originating from Caliente, with azimuths between 200-275°, has the potential to be explosion, rock fall, or PDC (Figure 6 b and c). Figure 6b shows a plot of $\boldsymbol{F}$ in slowness space with a peak in $\boldsymbol{F}$ at 270° over a short signal duration. I classify this as a Caliente explosion. Figure 6c has a longer duration and a signal with coherence spread through azimuths corresponding with the slopes of Caliente.

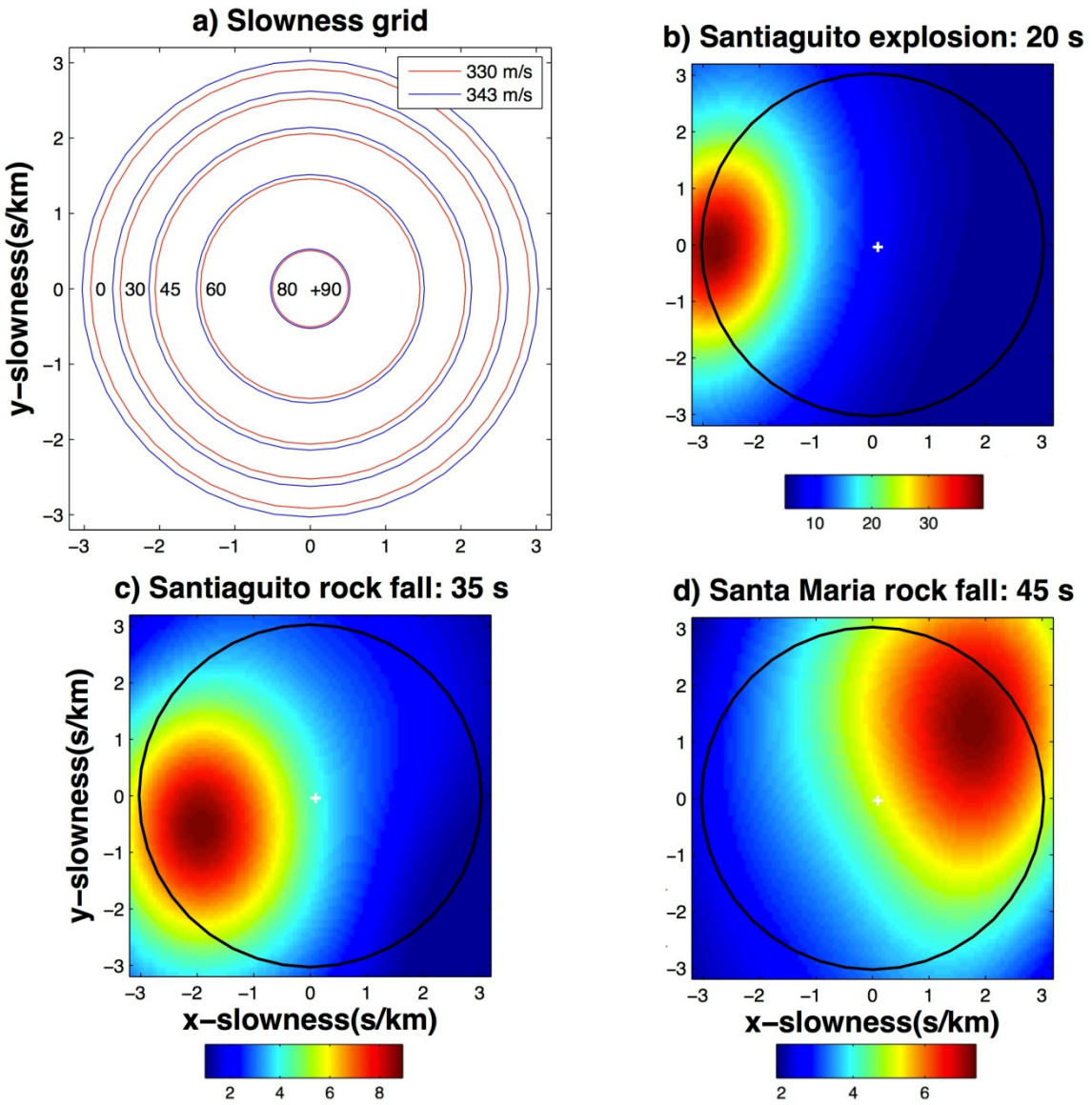

Figure 6. Slowness grid and coherence solution examples for three characteristic event types. Panel a) shows differences in elevation angle when using the high and low adiabatic sound speeds. Mean value of high and low adiabatic sound speed is used to calculate horizontal apparent slowness, shown as a black ring in b), c), and d). On b), c), and d), darker red indicates highest coherence, and dark blue represents none. Colorbars below each panel indicate *F* values for each particular plot.

Figure 6b shows easily identifiable characteristics of explosion signal. Short duration signals with high ***F*** such as this one occur in a range of azimuths from 259 to 270°. While energy arriving from this azimuth range may also contain rock falls, I use

only the azimuth for classification, and consider energy in this range to be explosion. Incoming energy with the backazimuth range of 200-258° will be classified as 'volcanic rock fall,' although this range may also contain PDC signal.

To begin separation of signal and noise, I will consider the range from 200-275° as volcanic and energy from Santa Maria, with the azimuthal range -45 to 95° as rock fall. Incoming energy from all other directions is classified as noise in this method. Figure 7 is a plot of all maximum ***F*** values of five-second windows, and their corresponding azimuths based on this classification method.

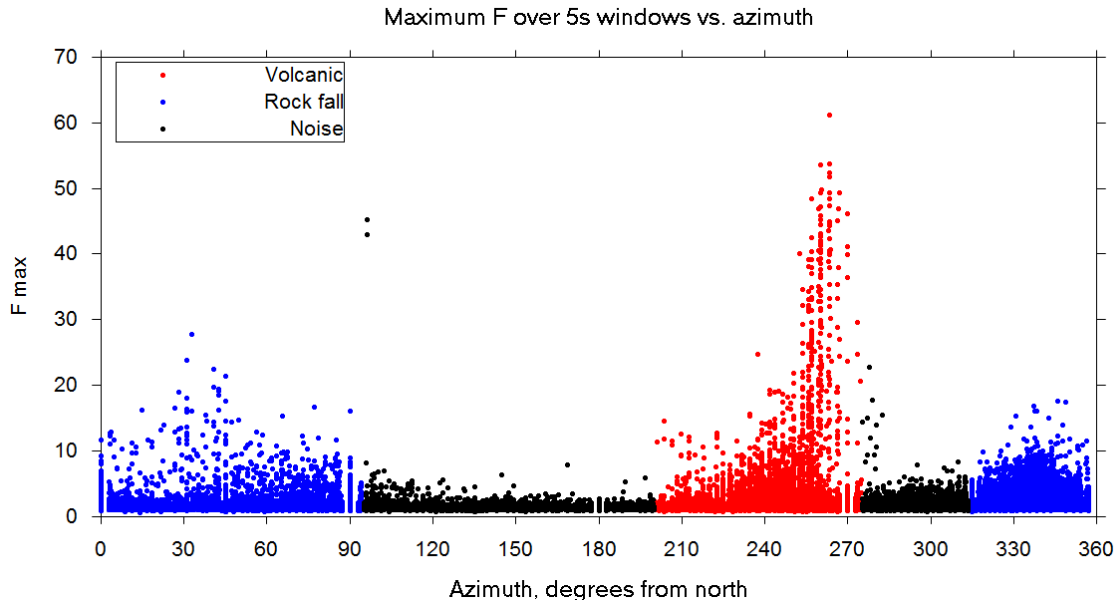

Figure 7. All calculated values of *F* plotted against azimuth. Red, blue, and black show azimuth-determined volcanic (rock fall and explosion sources together), rock fall (from Santa Maria) and non-signal azimuths (noise), respectively. *F* value here represents the max *F* value calculated for a 5-second window in the 0.25 - 20 Hz frequency band.

It is clear from Figure 7 that there are many windows from volcanic or rock fall directions with an ***F*** lower than the maximum ***F*** of noise in other windows. This suggests that there is a level of background noise at this site, originating from all

directions. In order to ensure differentiation between signal and noise within specified signal areas, I calculated an ***F***-threshold value.

A method used to determine an ***F***-threshold in previous studies was to calculate hypothetical ***F*** of random noise crossing an array (Almendros et al., 2002b). Almendros et al. calculated the probability density function (PDF) for these experimental noise detections, and then selected 95% of this value as a threshold. Anything above this value is treated as signal. In my study, however, ***F***-threshold calculation is less simple, because the level of background noise fluctuates from hour to hour, as can be seen in Figure 4. Figure 8 further demonstrates this discrepancy, showing the mean of ***F*** calculated for each window in an hour from the three different sources. In most hours, the ***F*** from Caliente and Santa Maria are higher than the mean ***F*** from noise.

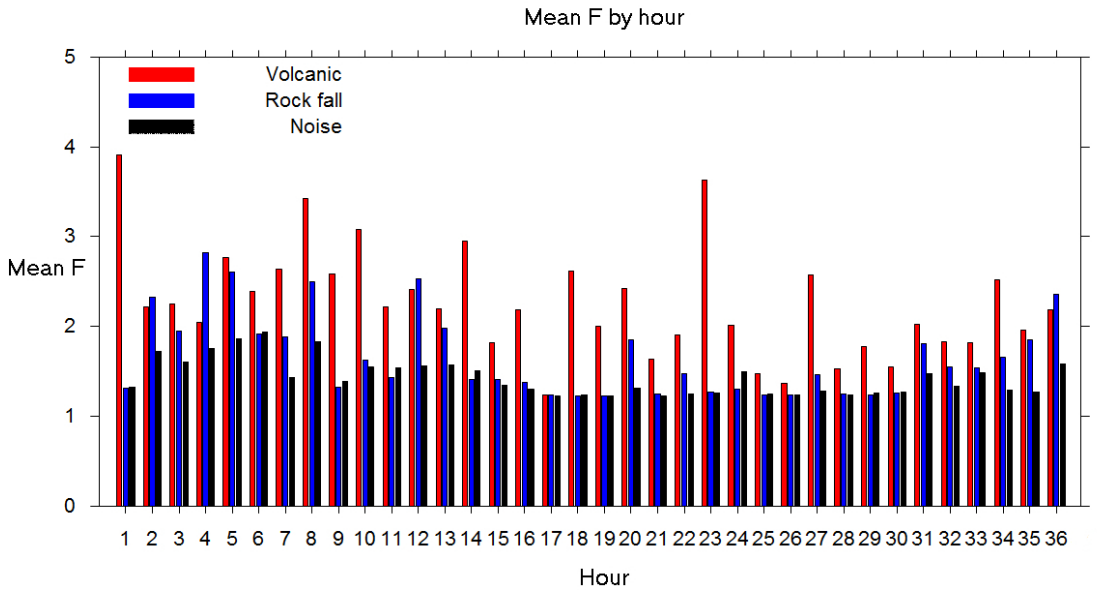

Figure 8. Mean *F* for each hour based on backazimuth-implied source. Bar colors correspond to volcanic (rock fall and explosions), Santa Maria rock fall, and noise (arriving from non-signal directions). Notice that mean value of *F* for noise changes by hour.

Because the level of noise appears to change every hour, simply creating random noise will not establish a sufficient ***F***-threshold value for the entire deployment. A moving ***F***-threshold that changes each hour is calculated to compensate for fluctuating levels of background noise. Each hour I used azimuth to separate out volcanic and rock fall signal from noise. I calculated a PDF for each signal type and each hour (Figure 9). In the hours shown, the most ***F*** from volcanic and rock fall signal occurs within the same range as noise. The figure shows that are still a number of events occurring above the highest noise value. These detections, above almost all events within the noise range, are the ones that should be considered signal. Choosing a threshold at 0.99 of the noise PDF's total value gives a 99% confidence in signal detections.

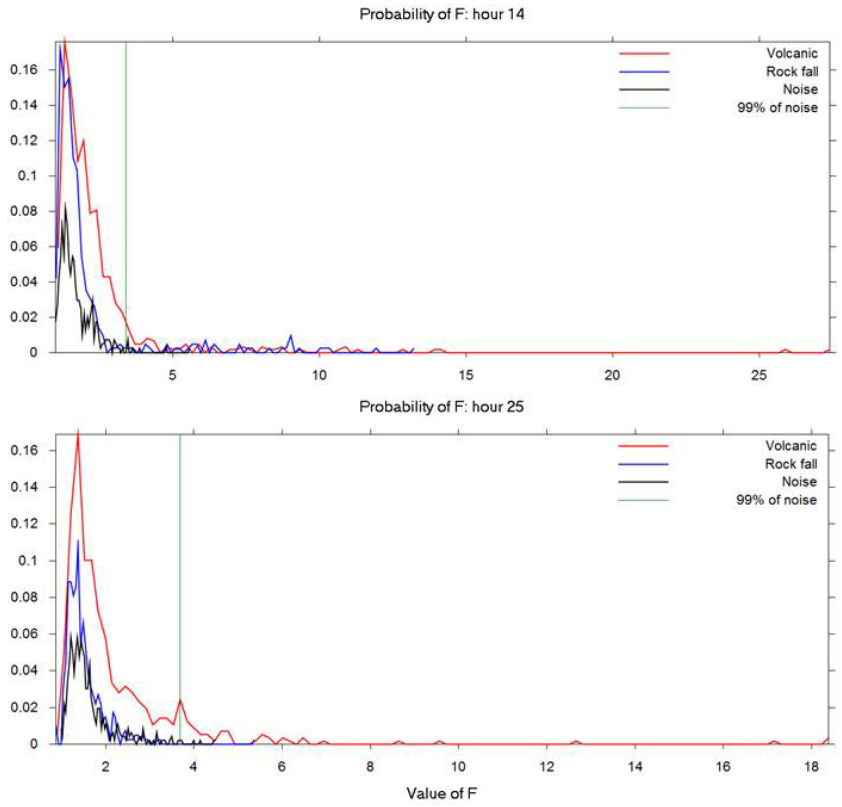

Figure 9. PDFs of volcanic, rock fall and noise sources, as determined by azimuth. *F*-threshold (vertical green line) is calculated at 99% of the noise PDF's total value to give 99% confidence that other values are above the noise level.

Many windows from signal directions are removed from the record by this ***F***-threshold. Figure 10 demonstrates the effectiveness of this threshold value by showing the new mean ***F*** for event detections per hour before and after an ***F***-threshold is implemented. Figure 11 provides additional proof by showing the number of windows with detection in each of the categories before and then after the implementation of an ***F***-threshold. There is a significant decrease in total number of detections, but there are far fewer detections remaining from noise azimuths.

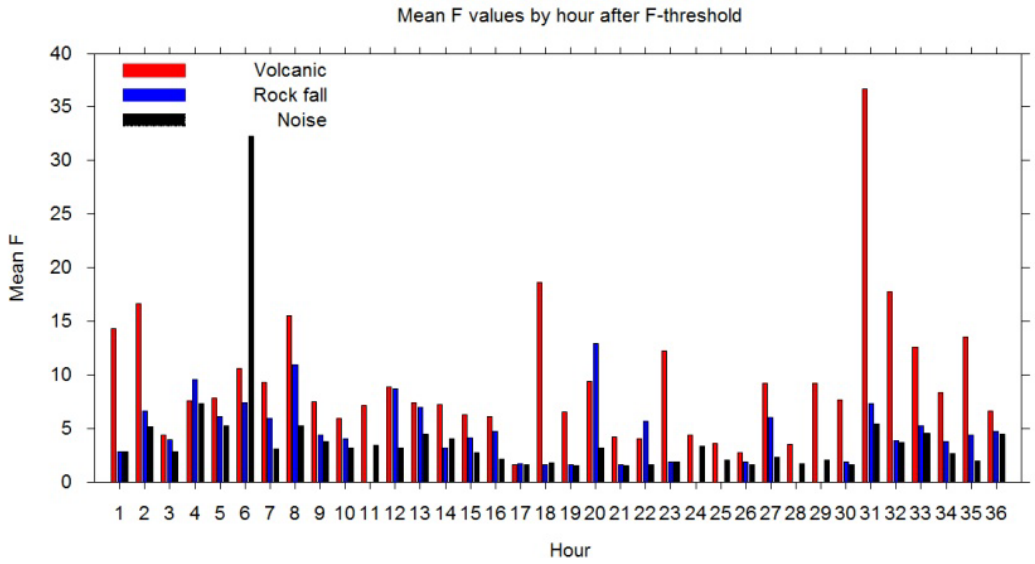

Figure 10. Mean values of *F* remaining after application of *F*-threshold. With 99% of the noise removed, only the highest *F*-thresholds remain, significantly increasing the mean of remaining signals.

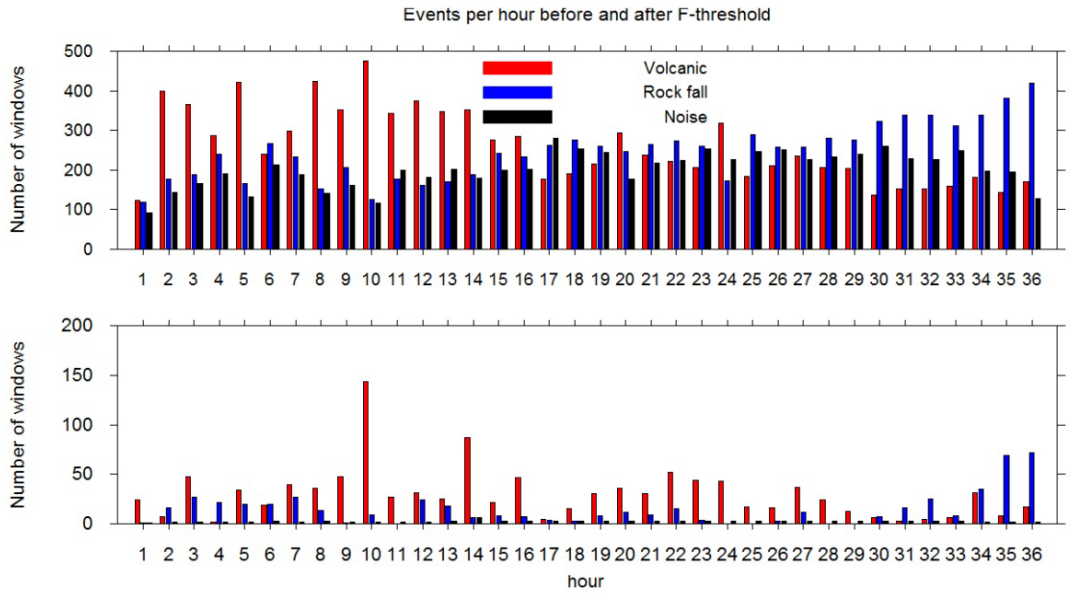

Figure 11. Number of detections each hour before (top) and after (bottom) an *F*-threshold is applied to the data. There are significantly fewer events, specifically from the noise directions in the later image, showing that the *F*-threshold was effective for decreasing the size of the dataset.

Once signal has been distinguished from noise, the next step is differentiating between moving and non-moving sources. In order to show spatial changes through time for the three signal types, I used beamforming and coherence analysis for each of the three type events (Figure 6 b-d) over short overlapping windows (figures 12, 13, 14). In each window, ***F***, azimuth, and elevation angle are calculated over 5 seconds of waveform. In order to achieve higher temporal resolution, time windows were overlapped by 90%, so each progressive value shown is 0.5 seconds after the previous window. The representation of motion in these figures provides a specific demonstration of how the signal changes over time, instead of the generalization averaged over the entire waveform shown in Figure 6.

I established error in azimuth and elevation angle in Figures 12-14 by using Monte Carlo simulations based on the bull's eye plots of Figure 6 (b, c, and d). For each

example in this figure, I calculated the azimuth and elevation angle of maximum ***F***, and standard deviation of the ***F*** distribution of the beam calculated by equation 6. This highest value is removed, and the process is repeated 89 times, to understand the distribution of ***F*** in slowness space. I chose 90 repeats to observe the spread of values over approximately the top 5% of ***F*** on a grid with 1764 total events (42x42 slowness grid). Error bars are plotted at one half the standard deviation in azimuth or elevation angle on either side of the signal.

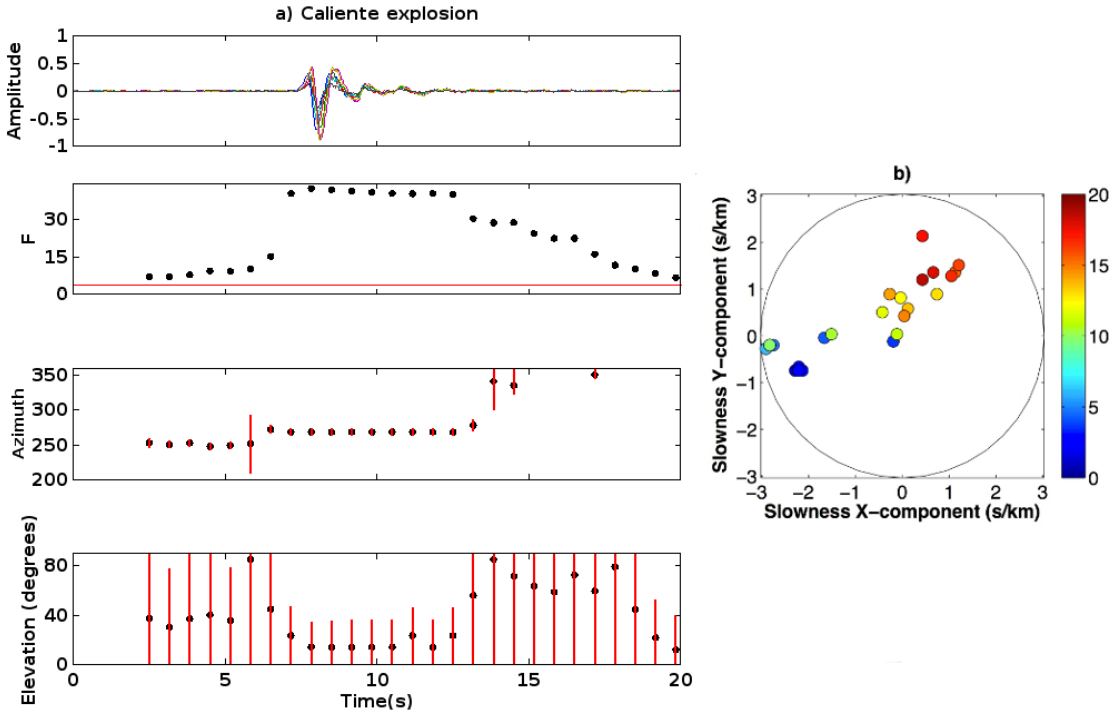

Figure 12. Example explosion event from Caliente with statistics tracked through time. Panel a) shows waveforms with normalized amplitude, *F*, azimuth and elevation angle over time, with red vertical lines indicating potential error for each window. Points indicate the center of a 5-second window. The red horizontal bar across the *F* window indicates *F*-threshold for this data. Azimuth panel is focused on the region of interest for the event, so that errorbars are visible. Panel b) shows slowness solutions of these events in time, with the colorbar representing time in seconds.

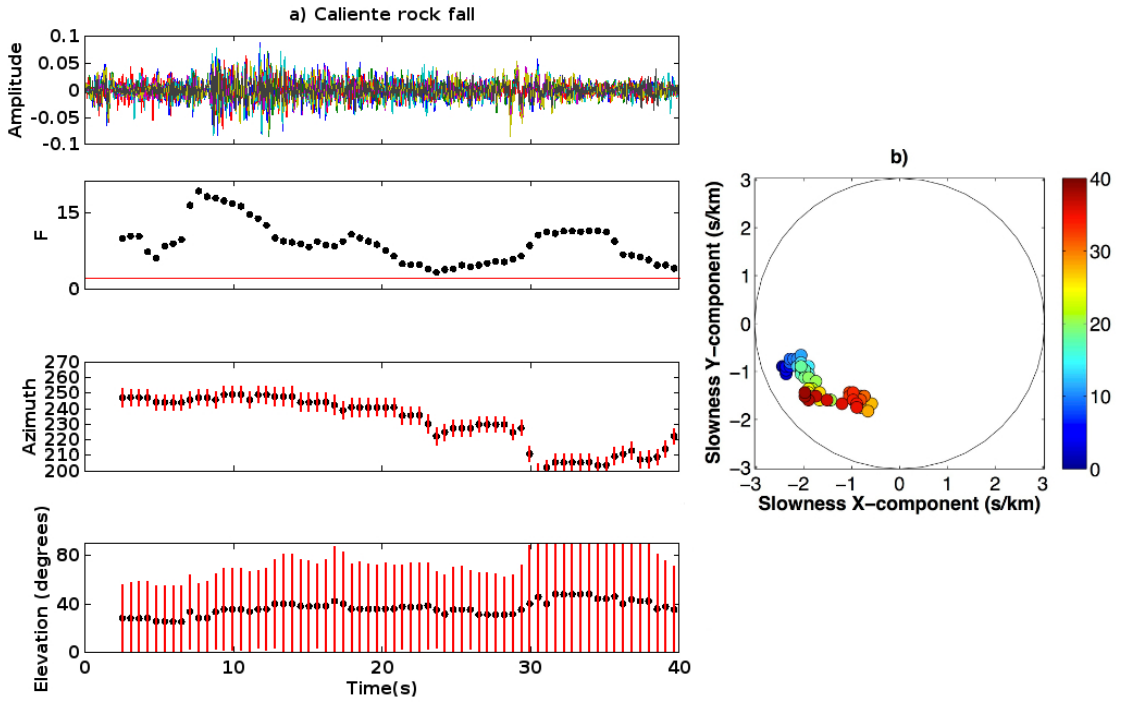

Figure 13. Example rock fall event from Caliente. All panels follow description from Figure 12. Azimuths are range-limited to show changes in azimuth over the progression of the event.

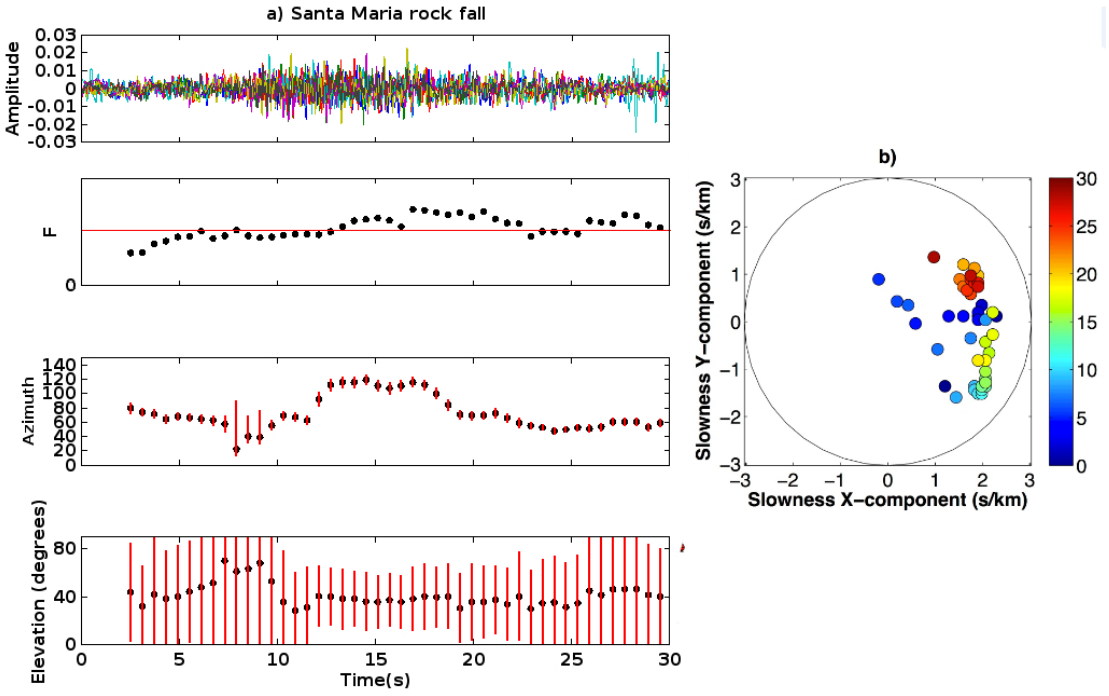

Figure 14. Characteristic Santa Maria rock fall event. All panels follow the description from Figure 12. Azimuth panel is range-limited to show region of interest.

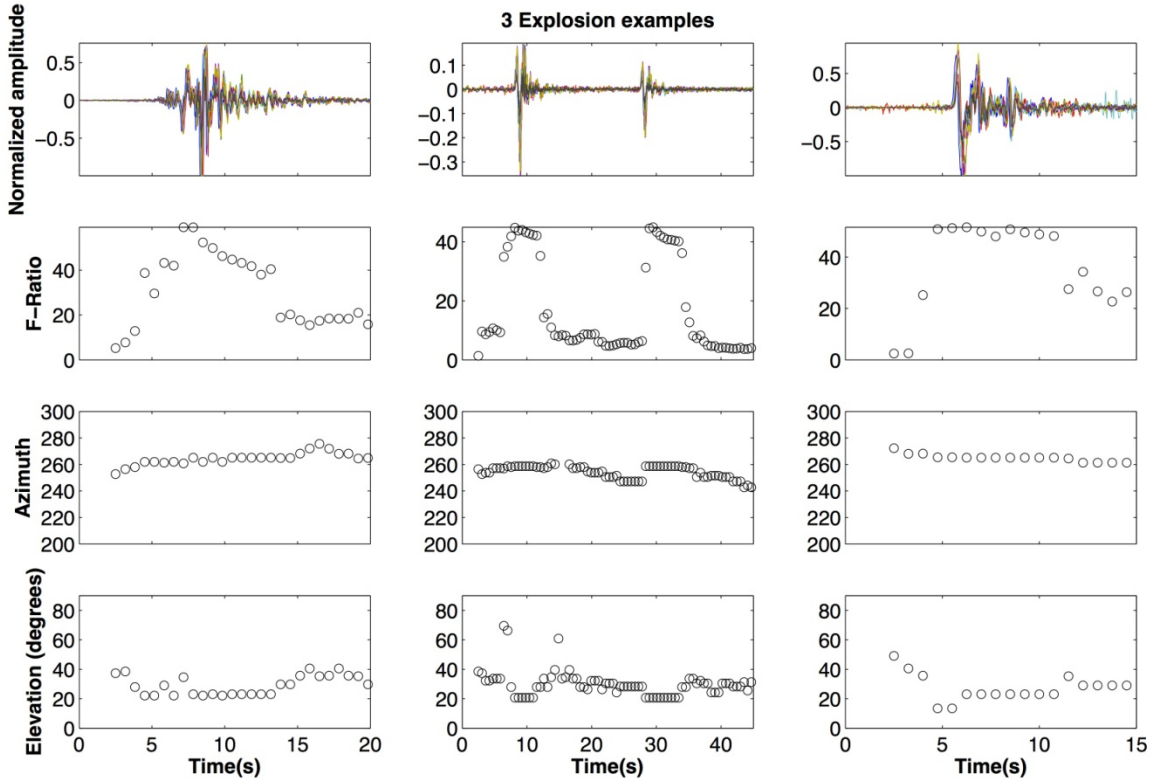

Figure 15. Three additional explosion examples. Waveform with amplitude (normalized to clipping amplitude), *F* and azimuth are plotted for each example, following the time scale on the bottom of the column. Plotted points indicate the center of a five-second window.

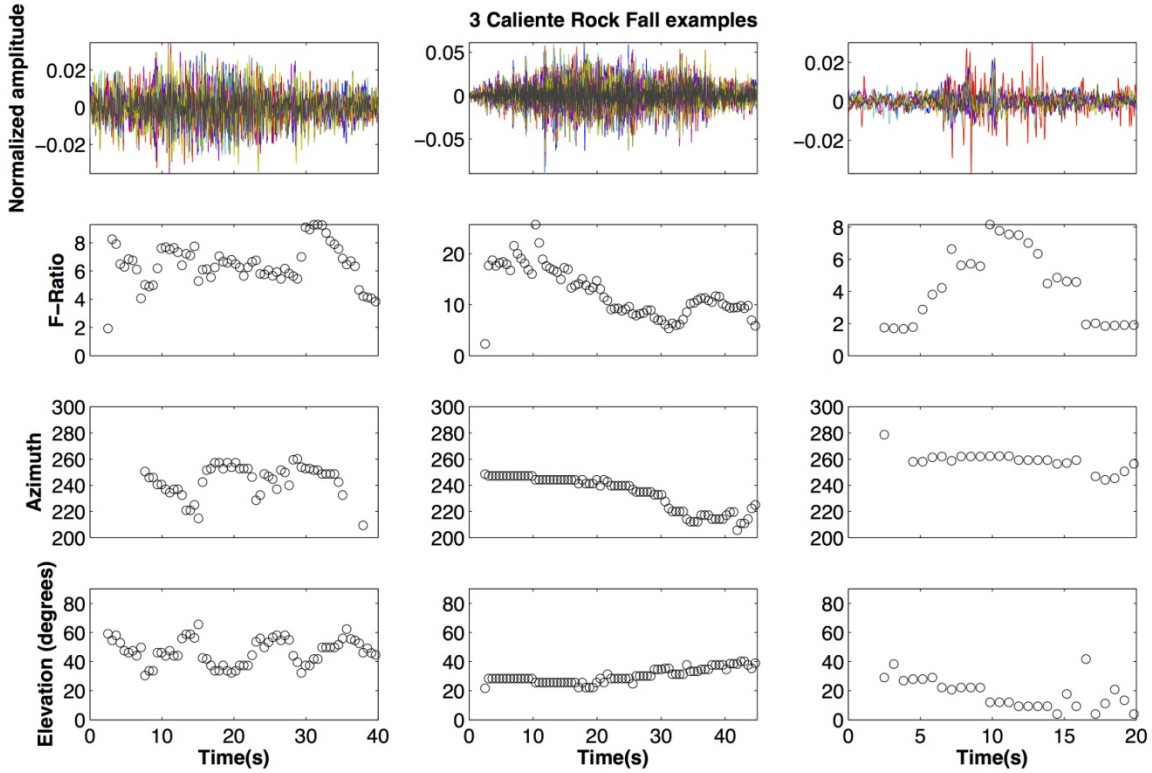

Figure 16. Three additional Caliente rock fall examples.

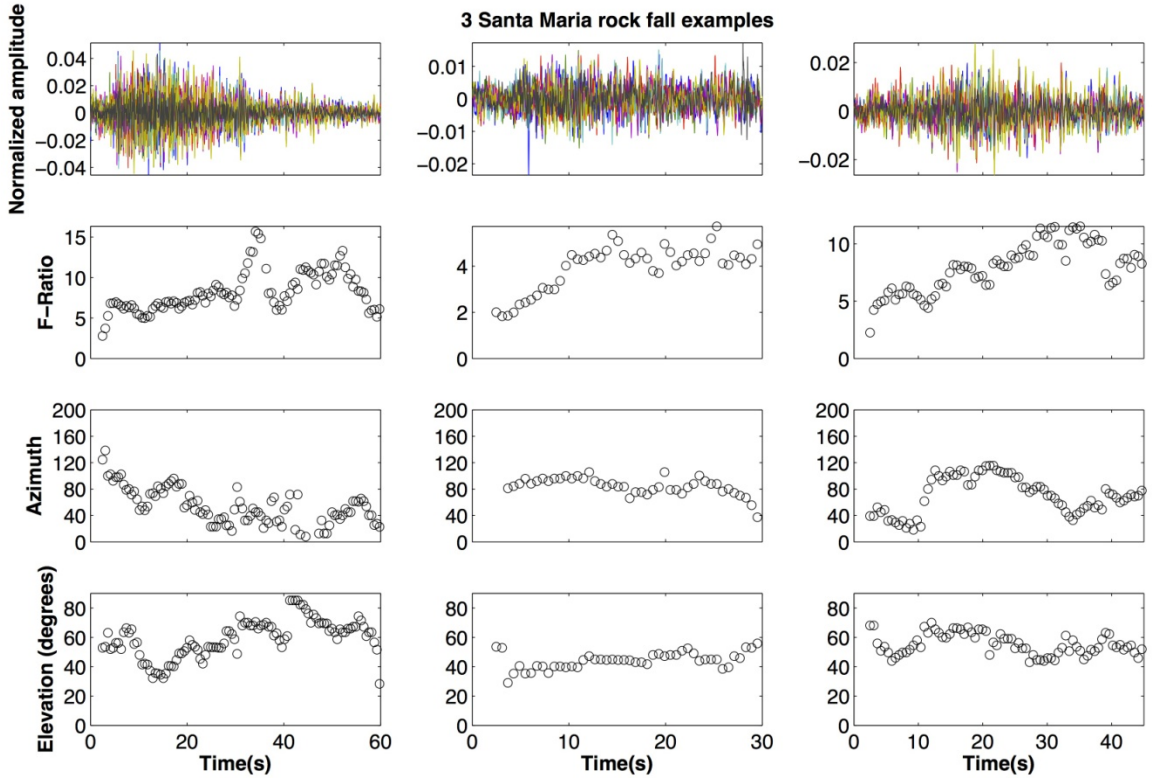

Figure 17. Three additional Santa Maria rock fall examples.

2.3 Results

Using beamforming and ***F*** calculation, I determined the number of event detections in each category per hour. After application of an ***F***-threshold to each specific window length and frequency band used, event types were separated by backazimuth. Total detections made in each category at different window lengths are below in Table 1.

Table 1. Windows with number of detected events in all search ranges. "Full" indicates 0.25-20 Hz band. Mean *F* value for each event type is also shown.

	Santa Maria RFs	Santa Maria RF ***F*** Mean	Caliente RFs	Caliente RF ***F*** Mean	Explosions	Explosion ***F*** Mean
5s Full	770	6.1	1260	6.7	212	20.9
5s 2-8 Hz	797	6.4	1178	6.9	325	17.0
10s Full	471	5.4	908	5.4	158	19.9
10s 2-8 Hz	522	5.5	841	5.6	227	15.9
30s Full	223	4.5	411	4.3	150	14.0
30s 2-8 Hz	338	4.6	421	4.23	152	13.8

Comparison of these different windows shows that adjusting the window length does affect the number of detections. In order to get a fair estimation of changes in detection between window lengths, Figure 18 shows percentage of windows with detections rather than number of detections, as in Table 1. Otherwise, the number of detections in the 5-second windows would be overrepresented just because there are more 5-second windows.

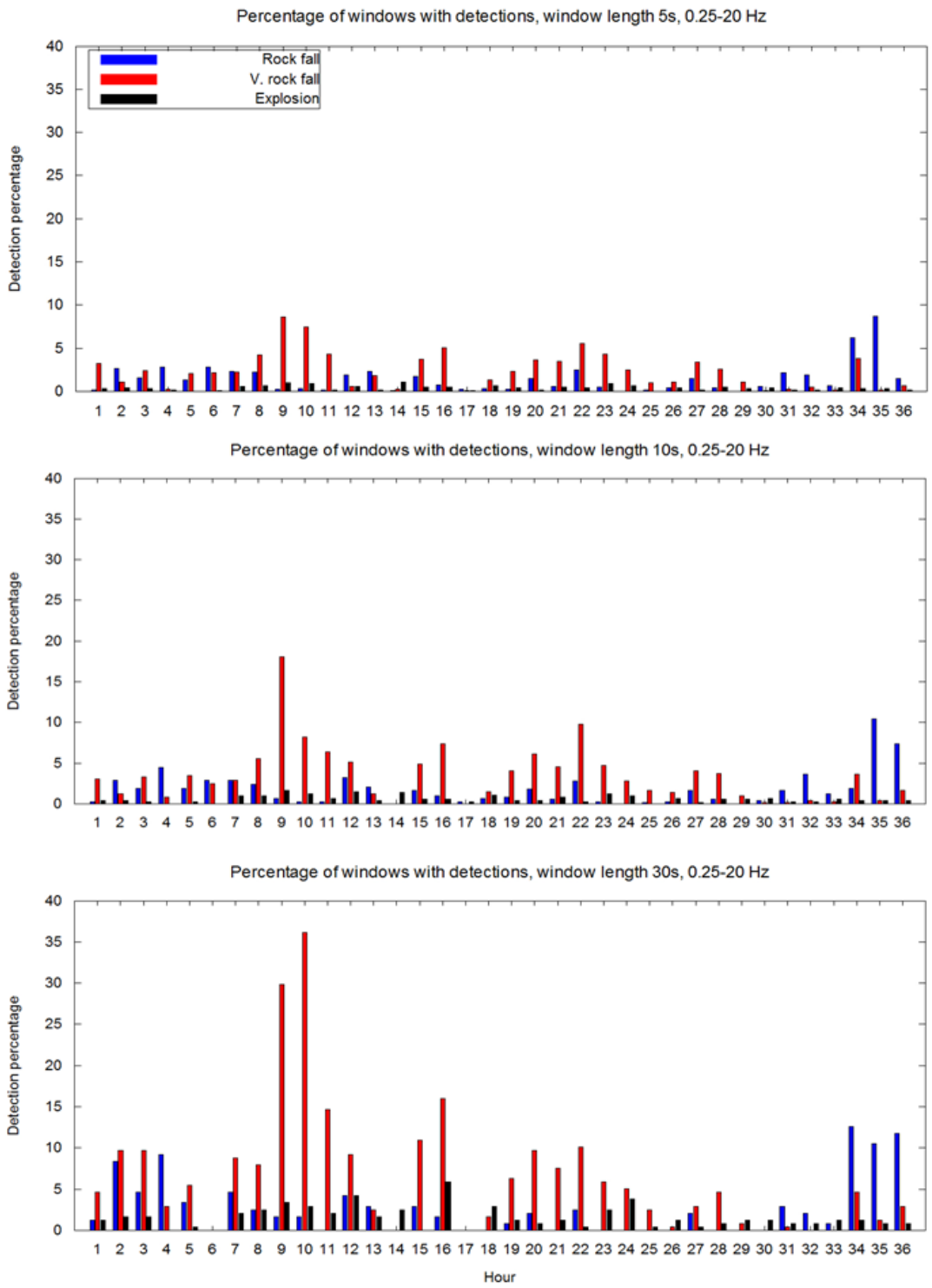

Figure 18. Comparison of event detections per hour at different window lengths. Figure shows 5, 10 and 30-second windows from top to bottom, respectively, and in the frequency band of 0.25-20 Hz. Colored bars indicate different sources, as shown in the legend of the first plot.

There is variation in number of detections between time windows. Overall, the greatest number of detections were rock fall from Caliente. Caliente rock falls were particularly high within 30-second time windows. Explosions make up the smallest percentage of most hours, and some hours of data contain no explosion signals at all. This result is consistent with observations of the volcano's activity, as explosions occur once every 0.5 to 2 hours.

For comparison of different frequency bands for detections, the 2-8 Hz frequency band, which is where previous studies have shown that rock fall signals contain energy (Luckett, 2002) was tested using the same process (Figure 19). Using this frequency band, the percentage of windows in which explosions are detected remains the same in each hour, but there is an increase in the number of volcanic and non-volcanic rock fall detections.

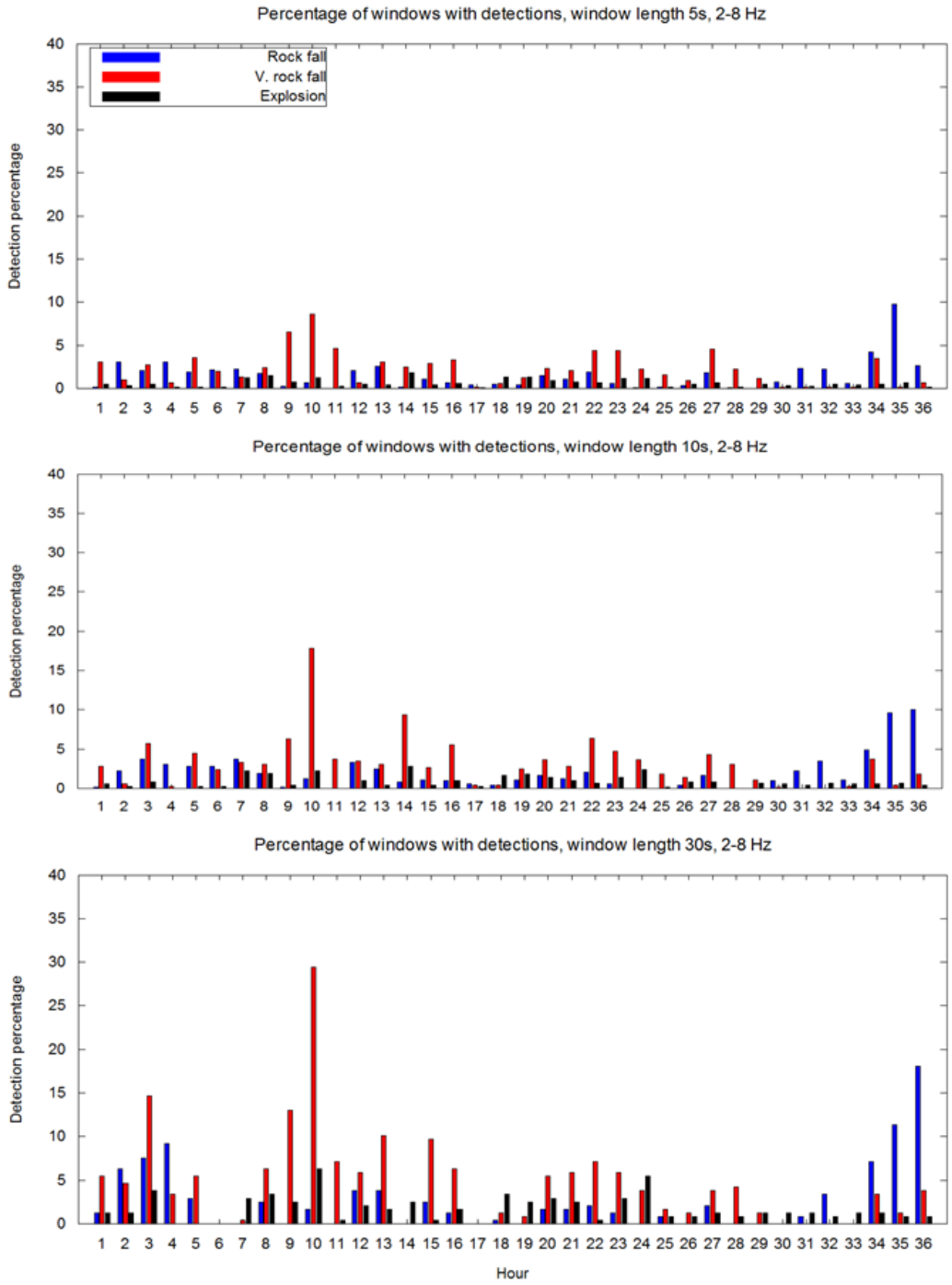

Figure 19. Detections per hour by event type (as in Figure 18), but in the 2 to 8 Hz frequency band. Detections are once again shown in the 5, 10, and 30s window lengths, from top to bottom, respectively.

I interpret this change in detections at different frequency bands as an indicator of a difference in spectral content between the rock fall and explosion signals. To test this hypothesis, a spectral median frequency is calculated for each window using the formula:

$$\boldsymbol{E_{SM}} = \frac{1}{2}\int_0^{f_{NYQ}} A_j \ \mathrm{d}f = \int_0^{f_{SM}} A_j \, df \tag{9}$$

where $\boldsymbol{E_{SM}}$ is the energy at the spectral median, $\boldsymbol{f_{NYQ}}$ is the Nyquist Frequency, 50 Hz, or one half of the sampling rate, $\boldsymbol{f_{SM}}$ is the spectral median frequency, and $\boldsymbol{A_j}$ is the value of the FFT of the waveform being calculated. The spectral median frequency is the frequency value at which $\boldsymbol{E_{SM}}$ is located.

This spectral median frequency is used as a representation of the midpoint in spectral energy of the time series. This value provides an estimate of what frequencies contain the most energy within the waveform. Spectral median frequencies are plotted against backazimuth in Figure 20, within the three window lengths. Events fall into different characteristic frequency bands, with explosions tending to have the lowest spectral medians. Spectral median for volcanic rock fall events is highest when azimuths are closest to the vent. Spectral median is lower as signal moves further from the vent.

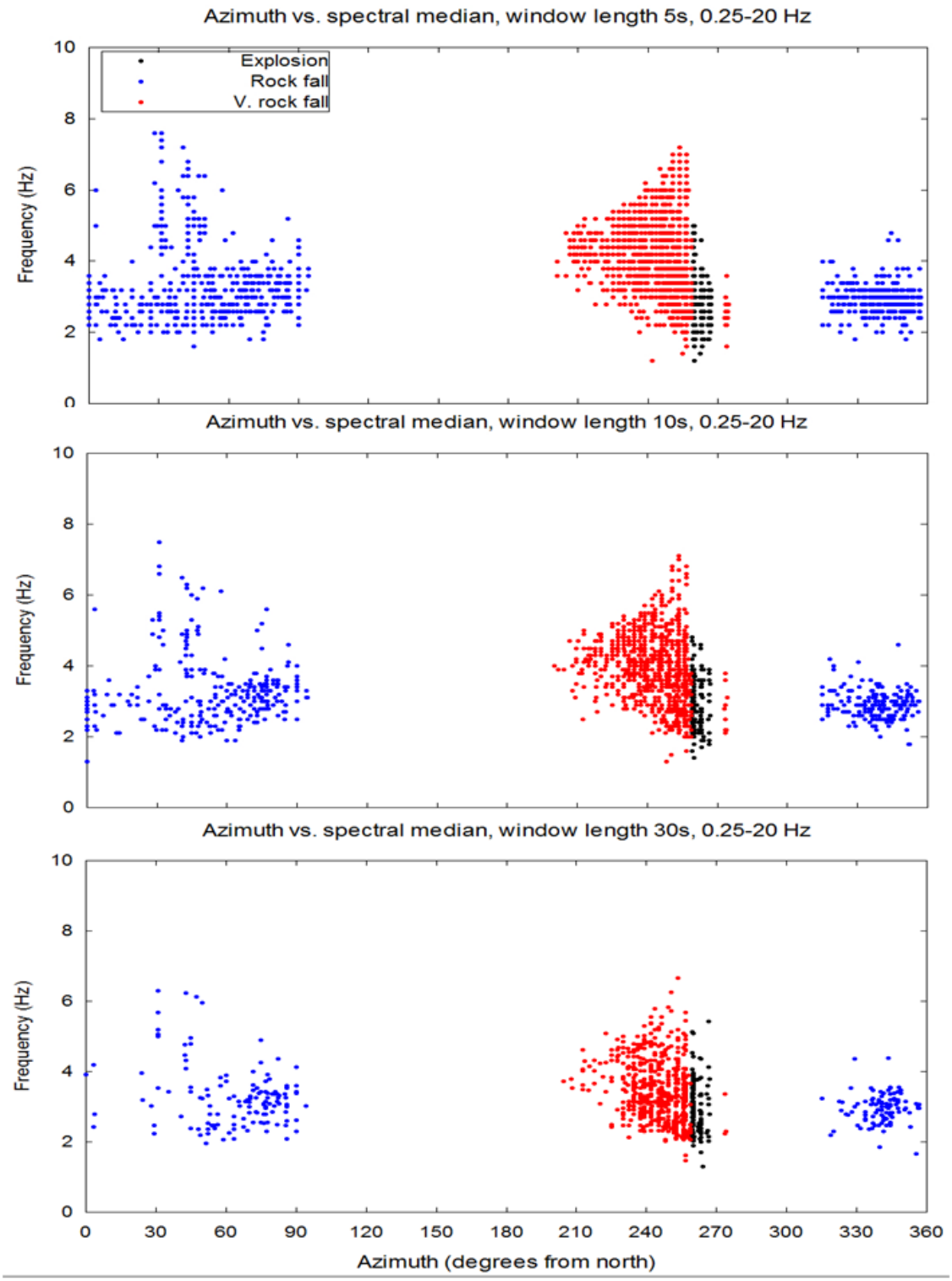

Figure 20. Comparison of spectral median frequency to azimuth. Comparisons are made in the full infrasound band at 5, 10, and 30 second window lengths from top to bottom, respectively.

CHAPTER THREE: DISCUSSION AND CONCLUSIONS

3.1 Discussion

3.1.1 Characteristic Identified Signals

The three signal types that have been identified are volcanic explosions, rock fall from Santa Maria, and rock falls from Caliente. Processing steps allow the determination of characteristics of these events, and the ability to differentiate between their signals.

Volcanic explosion signals stand out as the most identifiable. Figure 10 shows one of these events in detail. Clear explosion signals have high relative amplitude, often close to the clipping amplitude at 1. A high amplitude initial pulse is followed by oscillations with decreasing amplitude. The waveform is highly coherent across the array, with peaks and troughs of the signal appearing together on all seven channels with similar amplitude. High coherence is confirmed by the high $\boldsymbol{F}$ of this event. $\boldsymbol{F}$ is lower after the explosion, but remains at significant values of 5-15, possibly indicating the presence of a prolonged volcanic signal.

Evidence that explosion signal is a nonmoving source is seen in the azimuth and elevation angle plots (Figure 10). Santiaguito's vent is located at an azimuth of 259-270° from the array midpoint. Expected elevation angle between the array and the vent is just over 20°. In the explosion example, consistent azimuth values of 270 ± 5° occur from the very beginning of the window, even before the explosion waveform is seen. This potentially indicates some precursor signal originating from the volcano. Signal continues to have a high value of $\boldsymbol{F}$ and the same elevation angle after the explosion.

Signals during the eruption portion of the waveform also have the lowest errors, both in azimuth and in elevation angle. This is due to the high coherence of the waveform.

The remainder of the signal is characterized by changing backazimuths, ***F*** and elevations angles, which do not appear to have any consistent pattern. There is no coherent shape to the waveform towards the end of the signal. The low relative amplitude of other volcanic and non-volcanic signals compared to an explosion may make them too small to be visible on this plot. Three more explosions, and their characteristic elevation angle and backazimuths are shown in Figure 15.

A clear example of a moving source from Caliente, interpreted as a rock fall (Figure 11**),** has an emergent signal. Caliente rock falls do not immediately appear as strong signal but increase in amplitude over a few seconds. This 45-second window represents at least one rock fall event. The initial peak is the highest in both amplitude and ***F***. Throughout the waveform, smaller peaks appear in other coherent portions of the waveform, which is supported by the multiple peaks in the ***F*** plot.

Caliente rock fall signal's movement may be quantified by observing azimuth changes through the window. Azimuth begins near the vent around 250° and tracks to 235° over 30 seconds. These backazimuths are consistent with travel away from the vent and down the southeastern slope of the dome. Numerous rock falls were observed following this path during the deployment period. Blocks often break off the lava flow and tumble down the steep slope.

Calculated elevation angle data in this plot is inconsistent with downslope movement. Angle increases during the time when azimuth indicates that a source is traveling down the slopes of Caliente. Pairs of elevation angle above 20° and

backazimuths between 230-250° do not correspond to any physical locations along the dome. This pattern is also seen in elevation angles calculated for three more Caliente rock fall events (Figure 16). However, with the potential error in elevation angle being so high, it is probably safe to discount measurements of elevation angle for these waveforms as inaccurate.

A typical rock fall waveform from Santa Maria (Figure 12**)** shows a very similar, emergent, cigar-shaped waveform to those from Caliente. Signal begins around five seconds into the waveform, and increases to its maximum amplitude and ***F*** on all channels over the next few seconds. Backazimuths seen in Figure 14 and other rock fall signals **(**Figure 17**)** range between -45-95°.

Many rock falls from Santa Maria also show an increasing elevation angle over time. Unlike moving sources from Caliente, the elevation angles in this region actually could correspond to locations on Santa Maria, due to Santa Maria's height. Occasionally, rock falls began low on the slope, and were followed by rock falls higher up on the slope, so rising elevation angles on Santa Maria are not unrealistic. Once again, the high amount of error calculated for these events suggests that the elevation angle may not be a reliable measurement in this particular deployment, whether it corresponds to expected trends or not.

The relative abundance of these three types of signals also corresponds well to observations made in the field. Most detections originate from Caliente's slopes. During this period of high relative lava effusion, blocks breaking off of the lava flow were very common, whether an explosive eruption was occurring or not. Detections were also common from Santa Maria, where rock falls occurred frequently during the deployment,

but not as frequently as those from Caliente. However, due to their greater distance from the array, and a geometric spreading in acoustic amplitude with distance, these signals were weaker, which may have resulted in fewer detections.

Associated spectral medians of these three event types indicate trends in frequency content (Table 2). Based on these calculations, explosion signals have the lowest spectral median and volcanic rock falls consistently have the highest. The low frequency of explosions is consistent with other observations of volcanic explosions (Delle Donne et al., 2014; Johnson & Ronan, in review).

Table 2. Comparison of spectral median values. Mean and standard deviation of f_{SM} are shown for each window length.

	Santa Maria RFs: mean f_{SM}	Santa Maria RF: standard deviation of f_{SM}	Caliente RFs: mean f_{SM}	Caliente RF: standard deviation of f_{SM}	Explosion: mean f_{SM}	Explosion: standard deviation of f_{SM}
5s Full	3.20	0.87	4.24	1.0	2.90	0.68
10s Full	3.16	0.83	3.94	0.99	2.94	0.70
30s Full	3.15	0.73	3.48	0.86	2.97	0.71

3.1.2 Character of Rock Fall Signals

Knowing that signals originating from Santa Maria are almost guaranteed to be rock fall sources provides an excellent opportunity to observe characteristics of rock fall waveforms in detail. Waveforms in Figures 14 and 17 show four examples of the emergent nature of these signals. This signal type, and the cigar shape is noted as the shape of rock fall events in multiple studies. Amplitudes of these signals are relatively low when compared to most of the rock falls from Caliente.

There is a high possibility that there can be significant differences between any two rock fall waveforms due to the manner of infrasound generation from rock falls. Infrasound from rock falls is generated when rocks collide with the ground or other objects. A falling rock increases in velocity as it travels down a slope, increasing in kinetic energy. When this kinetic energy is transferred to another object via collision, collisions with higher velocity will create a higher amplitude signal. This is likely to contribute to the cigar shape of the waveforms. Amplitude begins low, and increases as the movement of rocks increases their total energy. Energy and amplitude then fall off slowly as individual rocks begin to lose velocity as the mass movement slows down.

Rock fall waveforms may also be influenced by the number and size of rocks within the flow. An individual rock tumbling down the slope will have a different waveform than that of many rocks traveling at once. Theoretically, larger, heavier blocks should also have higher amplitude signals, due to their higher mass resulting in a greater total kinetic energy. Without any specific observations to link rock fall size to signal in this deployment, it is difficult to compare how changing size and composition of rock falls affects the acoustic signal.

Rock falls from Santa Maria shown in Figure 20 have a wide range of spectral medians, though almost all of them fall in the predicted range between 2 and 8 Hz. In addition to spectral median, other measures can help to define the spectral character. I try to get a clearer picture of this energy distribution by calculating where the central 50% of energy is located. With alterations to Equation 9, I found the frequencies where 25% and 75% of the spectral energy were located for rock fall waveforms, instead of 50%, where f_{SM} is found. The difference between these two values is plotted as the middle 50% of spectral energy in Figure 21.

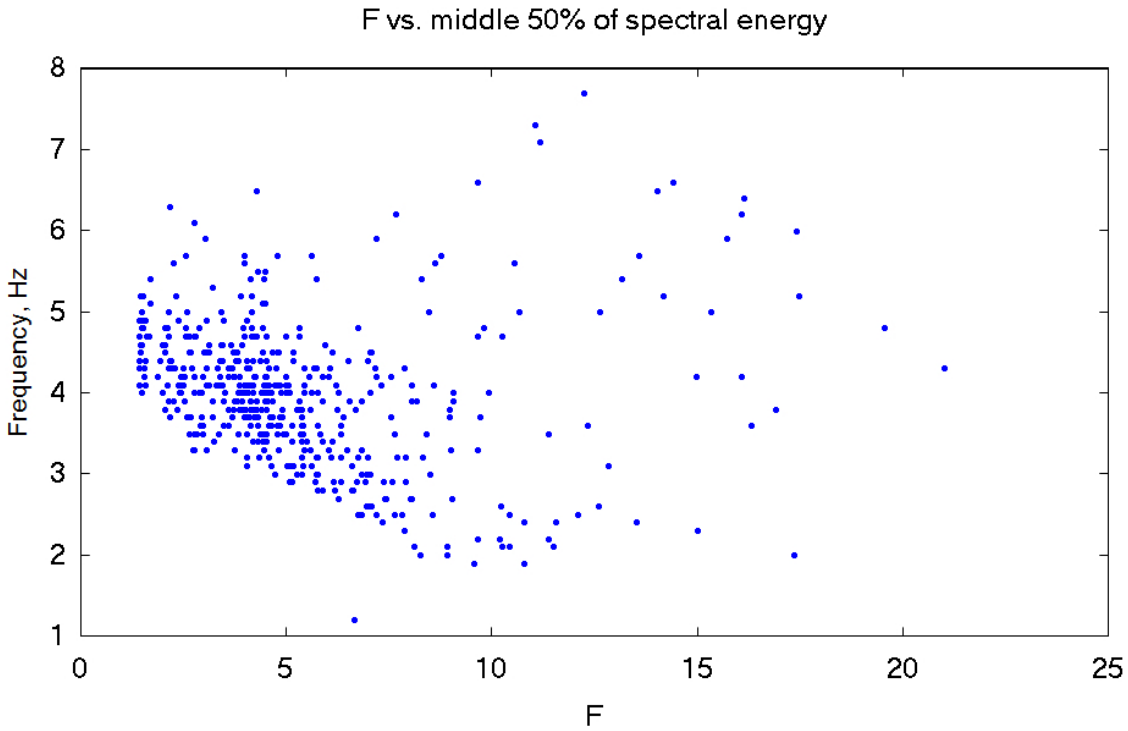

Figure 21. Width of center 50% of spectral energy of rock falls plotted against *F* value. Frequency is the difference between the 75th and 25th quantiles of energy, calculated in the same way as spectral median.

The middle 50% of spectral energy is an analog for the width of the spectra. It appears that there is a trend in signal with lower values of ***F*** having higher center widths,

and the width decreases with increasing signal coherence. However, the scattering of these points indicates that there is no strong trend.

The wide spread of values in rock falls from Santa Maria in Figures 20 and 21 show examples of how variable the spectra can be for these events. As mentioned above, the collisions between rocks and objects that generate infrasound are highly variable in time and space. The large differences in spectra are likely due to the high variability in actual rock falls, even when their waveforms the same general shape. It is possible to conclude from this that spectral character of rock fall events is too variable to be given a specific spectral range. However, the signals do seem to stay within the wider band described by Luckett (2002), of 2-8 Hz.

3.1.3 Other Detections and Interpretations

During the deployment, at least one event where an explosion was followed by a PDC was observed. Signal potentially corresponding to this type of event, showing characteristics of both an explosion and rock fall is seen in Figure 22. Location of maximum $\boldsymbol{F}$ was tracked through time using the same process as above. The signal remained fixed in azimuth during the highest amplitude portion, corresponding to an explosion. Azimuth then decreased gradually, corresponding to a progression down the slope, which is characteristic of signal previously identified as volcanic rock fall in this experiment.

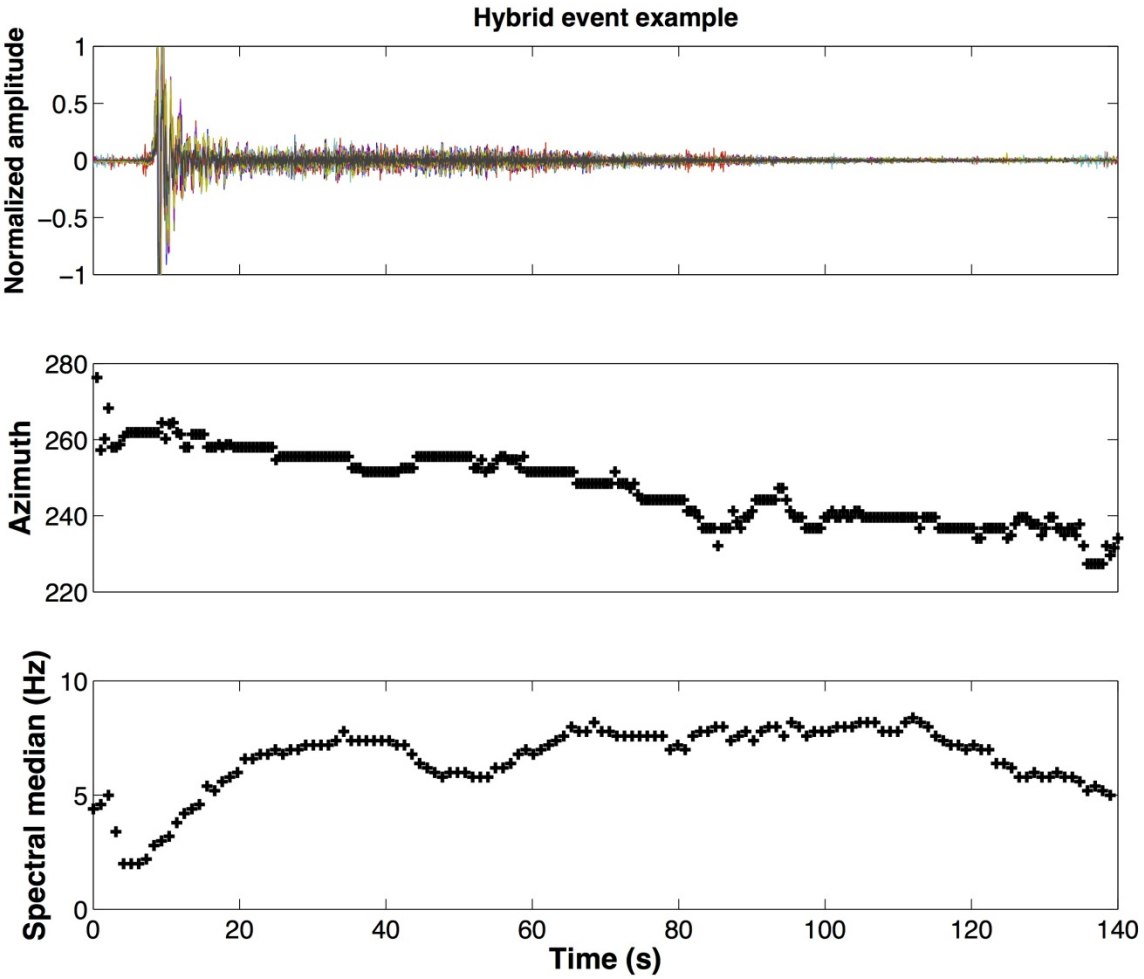

Figure 22. Time series analysis for a hybrid event. Waveform, backazimuth and spectral median are plotted over 140 seconds. Each point represents the center of a 5-second window with 90% overlap, like those used in Figures 10-15.

I interpret this "hybrid" signal, as an explosion followed by a larger gravity-flow event, which could be a rock fall or PDC. Amplitude and coherence of this signal over time are higher than many of the rock falls observed on Caliente and the azimuth consistently shifts further down the slope. Details about this event are comparable to a PDC detected at Soufriere Hills Volcano, which was triggered by a column collapse (Delle Donne et al., 2014). In the Soufriere Hills Volcano PDC, the explosion portion of the waveform had a low frequency. This was followed by an increase in frequency as the column collapsed, and a PDC initiated. The sustained higher spectral median calculated

in my signal as it moves away from the vent is consistent with these observations. While the magnitude of the Caliente event is significantly smaller, it is likely that the two event types would show similar spectral characteristics. An event of this type at Caliente was detected, and confirmed with video in the 2014 deployment (Johnson & Ronan, in review). Similarly, frequency values were low for the explosion, then increased as the PDC began to move down the hill.

I propose that portions of this hybrid signal immediately following the explosion may also be from falling ballistics. Azimuths of highest ***F*** in the five seconds immediately following the explosion signal occur both north and south of the azimuth of the volcano. Ballistic ejection is common during explosions from Caliente. When observing the eruptions, it was clear that the largest ballistic blocks fall closest to the vent, but are not necessarily directed to any specific slope. These blocks would fall on either side of the volcano causing fluctuating azimuths for the first 5 seconds after the explosion. These blocks and other smaller ballistics rolling downslope could also initiate rock falls.

Another type of detected event was interpreted as an echo from an explosion. After some explosions, areas of coherent signal were detected from the direction of Santa Maria, 10 seconds after the explosive impulse (e.g., Figure 12). This signal is lower amplitude than the explosion in the window, but has a small spike in ***F*** from the direction on Santa Maria's slopes. Distance from the vent to the detected azimuth on Santa Maria and back to the array is approximately 3000 meters with some variation due to the height of Santa Maria. At an assumed sound speed of 330 m/s, an echo signal should reach the array at around 9 seconds after the explosion, which fits this dataset.

Other uncharacterized detections were the longer duration, non-moving signals from Caliente. With durations of 5-30 seconds, and relative amplitudes of 0.5 or higher, these sources did not fit the typical impulsive explosion category. Based on my field observations, I propose that these detections correspond to periods of gas jetting. Gas jetting is a common phenomenon that has been observed by others in the field **(**Johnson et al., 2011).

3.1.4 Wind and Atmospheric Noise

Wind noise was also common in portions of the record, which made detection of signals difficult. Figure 4 shows that the period of highest winds occurs during hours 28-32. During this time period, very few detections of rock falls occurred. Figure 8 shows that ***F*** calculated for even high coherence events, such as explosions, were lower in this period than in calm hours. Figure 8 also shows that there was a higher mean ***F*** for noise sources during hours 29 and 31. Lower signal to noise ratios during these periods of high wind caused fewer detections of events. This is backed up further by the record shown in Figures 18 and 19. Some hours during the windy period contain zero detections of rock falls, even when the signal is filtered to the 2-8 Hz band, to better constrain rock fall signal.

Increased ***F*** values of noise during some time periods indicates that there is coherence to some sources of noise. If energy from noise was entirely incoherent and random, there would be no need to create a moving ***F***-threshold value. While the adjusted ***F***-threshold removes noise from the directions of expected signal in these cases, it also cuts signal, reducing the number of detections. There is a 99% confidence with the ***F***-threshold that detections are truly detections, but when the noise level is higher, some

more event detections will be cut off by the high threshold as well. This is mainly noted as an inconvenience of working with infrasound in high noise environments.

Another type of atmospheric noise that is commonly observed in infrasound deployments is microbaroms. Microbaroms are a continuous acoustic oscillation in the atmosphere from the rise and fall of ocean waves, with a period from 5 to 8 seconds, or frequencies of 0.125-0.2 Hz (Hedlin et al., 2002). Over long-term deployments, microbaroms often dominate the power spectrum of infrasound energy, due to their continuous propagation.

In this particular deployment, I suggest that microbaroms will not have a large effect on the spectra. Over 5, 10, and 30 second windows, few microbarometric oscillations occur, resulting in a low acoustic power compared to local sources. Due to the low-frequency rolloff in ECMs, the amplitudes of low-frequency microbaroms will be low on these recordings, even when they are detectable. Furthermore, the bandpass filter I used in this experiment filtered data between 0.25 and 20 Hz, cutting off the frequency range where microbaroms occur.

3.1.5 Future Work

Characteristics of known rock falls were determined using an array of ECMs on signals known to be originating from Santa Maria's slopes. Moving events from Caliente were assumed to be rock falls in most cases, though during the deployment, I observed several PDCs. Differentiation between these two sources is difficult to confirm without the use of other observational methods. The hybrid event in Figure 22, for example, requires more information to be able to prove exactly what caused it. The beginning of the signal is easily characterized as an explosion, but the later section could be attributed

to a number of sources, including PDC, ballistic fall, and rock fall. Without visual confirmation, definite statements about these events are not possible to back up with evidence.

Improvements to this study were made in a second deployment in January 2014, when an array of infrasound microphones were deployed alongside a time-synchronized camera (Johnson & Ronan, in review). Through the brief period where the mountain was not obscured by clouds, many rock falls, several explosions, and one small PDC were observed. Comparing these time windows to infrasound signals processed in the same way will determine if there are infrasonic signal character differences between pure rock falls and PDCs. To make definite conclusions, a larger sample size may be needed.

Differentiation of these sources with purely infrasound records could prove useful in long-term volcanic observation. Infrasound can provide a record of surface events, even when the volcano is obscured, or during adverse weather (Ripepe et al., 2010). Observation of long-term trends in volcanic activity could be performed on a daily or hourly scale, when tracking known event sources by azimuth. Remote event detection has already been useful for representing volcanic activity at multiple volcanoes (Luckett, 2002; Hibert et al., 2014).

3.2 Conclusion

A standalone array of infrasound-sensitive ECMs is able to identify moving sources at Santiaguito through array processing. Beamforming and calculating $\boldsymbol{F}$ in the frequency domain is an effective way to locate the most coherent energy. Tracking this movement through time using overlapping windows shows a progression of backazimuths and indicates source movement. Signal is characterized into the three

event types, volcanic rock fall, non-volcanic rock fall, and volcanic explosions using known azimuths for event types as determined by backazimuth.

Volcanic rock falls were the most often detected event. Both volcanic and non-volcanic rock falls show change in azimuth over time and a higher value of spectral median. Rock falls from Santa Maria are consistently lower in amplitude than those from Caliente. The lower amplitude of Santa Maria signals may have resulted in fewer detections of these events during periods of high wind noise. Spectral median calculated for rock falls from Santa Maria and Caliente sources seems to indicate that the two sources have similar spectral character.

Other signals which are less common, but distinct, are attributed to volcanic explosions. Several PDCs were also observed in the field, but their signals are difficult to distinguish from volcanic rock falls when using infrasound alone. The highest spectral medians from azimuths of Caliente's slopes were located closest to the vent. This could be due to PDCs, which have been shown to have a higher frequency than explosions (Delle Donne et al., 2014; Johnson & Ronan, in review). I suggest that they could also be due to ballistic fall, and associated rock fall, which are also known to have a higher frequency content than explosions (Luckett, 2002).

Arrays of ECMs allow an effective means to track the locations of rock fall events and explosions through time on a volcano. Due to their low cost, these microphones could be useful for deployment in many remote locations where active volcano monitoring is needed. However, in order to fully understand the signals contained in infrasonic records, further research including time-synchronized video observations

would be necessary to conclusively differentiate between moving sources such as rock fall, PDC, and ballistic fall.

REFERENCES

Almendros, J., Chouet, B. A., & Dawson, P. B. (2002a). Array detection of a moving source. *Seismological research letters*, 73(2), 153-165.

Almendros, J., Chouet, B. A., Dawson, P. B., & Huber, C. (2002b). Mapping the sources of the seismic wave field at Kilauea volcano, Hawaii, using data recorded on multiple seismic antennas. *Bulletin of the seismological society of America*, 92(6), 2333-2351.

Bluth, G. J. S., & Rose, W. I. (2004). Observations of eruptive activity at Santiaguito volcano, Guatemala. *journal of volcanology and geothermal research*, 136(3-4), 297-302.

Caljé, L. (2005). Exploring boundaries of the fisher and PMCC signal-detectors using infrasound signals (Doctoral dissertation, Master's thesis, University of Utrecht/Royal Dutch Meteorological Institute (KNMI)).

Cansi, Y. (1995). An automatic seismic event processing for detection and location; the P.M.C.C. method. *Geophysical research letters*, 22(9), 1021-1024.

Carn, S. A., Watts, R. B., Thompson, G., & Norton, G. E. (2004). Anatomy of a lava dome collapse; the 20 march 2000 event at soufriere hills volcano, montserrat. *Journal of olcanology and geothermal research, 131*(3-4), 241-264.

Delle Donne, D., Ripepe, M., De Angelis, S.,M.H., Cole, P. D., Lacanna, G., Poggi, P., & Stewart, R. C. (2014). Thermal, acoustic and seismic signals from pyroclastic density currents and vulcanian explosions at Soufriere Hills volcano, Montserrat. *Memoirs of the geological society of London, 39*, 169-178.

Evers, L., & Schweitzer, J. (2011). A climatology of infrasound detections in northern Norway at the experimental ARCI array. *Journal of seismology, 15*(3), 473-486.

Garces, M. A., Hansen, R. A., & Lindquist, K. G. (1998). Traveltimes for infrasonic waves propagating in a stratified atmosphere. *Geophysical journal international*, 135(1), 255-263.

Harris, A., Flynn, L., Matias, O., & Rose, W. (2002). The thermal stealth flows of Santiaguito dome, Guatemala: Implications for the cooling and emplacement of dacitic block-lava flows. *Bulletin of the geological society of America*, 114(5), 533-546.

Harris, A. J., Rose, W. I., & Flynn, L. P. (2003). Temporal trends in lava dome extrusion at Santiaguito 1922-2000. *Bulletin of volcanology*, 65(2-3), 77-89.

Havens, S., Marshall, H. P., Johnson, J. B., Nicholson, B. (2014). Calculating the velocity of a fast moving snow avalanche using an infrasound array. *Geophysical Research letters*, 41(17), 6191-6198.

Hedlin, M., Berger, J., & Vernon, F. L. (2002). Surveying infrasonic noise on oceanic islands. *Pure and applied geophysics*, 159(5), 1127-1152.

Hibert, C., Mangeney, A., Grandjean, G., Baillard, C., Rivet, D., Shapiro, N. M., . . . Crawford, W. (2014). Automated identification, location, and volume estimation of rockfalls at piton de la fournaise volcano. *Journal of Geophysical Research: Earth Surface, 119*(5), 1082-1105.

Holland, A. S. P., Watson, I. M., Phillips, J. C., Caricchi, L., & Dalton, M. P. (2011). Degassing processes during lava dome growth; insights from Santiaguito lava dome, Guatemala. *Journal of volcanology and geothermal research*, 202(1-2), 153-166.

Hort, M., Voege, M., Seyfried, R., & Ratdomopurbo, A. (2006). In situ observation of dome instabilities at Merapi volcano, Indonesia; a new tool for volcanic hazard mitigation. *Journal of volcanology and geothermal research, 153*(3-4), 301-312.

Johnson, J. B., Aster, R. C., Ruiz, M. C., Malone, S. D., McChesney, P. J., Lees, J. M., & Kyle, P. R. (2003). Interpretation and utility of infrasonic records from erupting volcanoes. *Journal of volcanology and geothermal research, 121*(1), 15-63.

Johnson, J. B., Lees, J., & Varley, N. (2011). Characterizing complex eruptive activity at Santiaguito, Guatemala using infrasound semblance in networked arrays. *Journal of volcanology and geothermal research*, 199(1-2), 1-14.

Johnson, J. B., Ronan, T.R. (in review), Infrasound from volcanic rockfalls. *Journal of geophysical research*.

Luckett, Rich (2002). "The relationship between degassing and rockfall signals at Soufriere Hills volcano, Montserrat". *Memoirs of the geological society of London*, 21(1), 595-602.

Melton, B. S., & Bailey, L. F. (1957). Multiple signal correlators. *Geophysics*, 22(3), 565-588.

Moran, S. C., Matoza, R. S., Garces, M. A., Hedlin, M. A. H., Bowers, D., Scott, W. E., Vallance, J. W. (2008). Seismic and acoustic recordings of an unusually large rockfall at Mount St. Helens, Washington. *Geophysical research letters*, 35(19).

National Earthquake Information Center (NEIC). (2012). *M 7.4 – offshore Guatemala. Retrieved from* http://earthquake.usgs.gov/earthquakes/eventpage/usp000jv5f#general_summary

Okuno, T., Saito, M., Ikeda, K., Sato, T., & Okuma, S. (2001). Study on collapse of the lava dome, unzen volcano using the airborne geophysical survey method. *Bulletin of the geological survey of Japan*, *52*(2-3), 113-124.

Ripepe, M., Angelis, S. D., Lacanna, G., & Voight, B. (2010). Observation of infrasonic and gravity waves at Soufriere Hills volcano, Montserrat. *Geophysical research letters*, 37(19).

Rose, W. I. (1987). Volcanic activity at Santiaguito volcano, 1976-1984. *Special paper - geological society of America*, 212, 17-27.

Rost, S., & Thomas, C. (2002). Array seismology; methods and applications. *Reviews of geophysics*, 40(3), 2-1.

Ruiz, M. C., Lees, J. M., & Johnson, J. B. (2006). Source constraints of Tungurahua volcano explosion events. *Bulletin of volcanology*, *68*(5), 480-490.

Scott, J. A. J., Pyle, D. M., Mather, T. A., & Rose, W. I. (2013). Geochemistry and evolution of the Santiaguito volcanic dome complex, Guatemala. *Journal of volcanology and geothermal research*, 252, 92-107.

Singer, B. S., Smith, K. E., Jicha, B. R., Beard, B. L., Johnson, C. M., & Rogers, N. W. (2011). Tracking open-system differentiation during growth of Santa Maria volcano, Guatemala. *Journal of petrology*, 52(12), 2335-2363.

Smart, E., & Flinn, E. A. (1971). Fast frequency-wavenumber analysis and Fisher signal detection in real-time infrasonic array data processing. *Geophysical journal international*, 26(1-4), 279-284.

Yamasato, H. (1997). Quantitative analysis of pyroclastic flows using infrasonic and seismic data at Unzen volcano, Japan. *Journal of physics of the earth*, 45(6), 397-416.